

Multi-channel rank reduction methods with applications to  
receiver function reconstruction

by

Gonzalo Rubio

A thesis submitted in partial fulfillment of the requirements for the degree of

Master of Science  
in  
Geophysics

Department of Physics  
University of Alberta

©Gonzalo Rubio, 2020

# Abstract

Modern exploration seismology acquires data that depend on four spatial variables ( $x - y$  source and receivers coordinates) and time. Each recorded seismogram belongs to a source-receiver pair defined by their spatial coordinates. The distribution of source and receiver on the surface of the Earth is often irregular, however, and thus reconstruction methods are adopted to simultaneously denoise and regularize the seismic survey. Data reconstruction is nowadays a customary step for preconditioning exploration seismology records. Despite the popularity of reconstruction techniques for processing exploration seismic data, they have not become a standard processing tool for global seismological data.

The goal of this thesis is to develop and evaluate reconstruction techniques as a means to enhance data acquired by seismological networks. The work focuses on Multichannel Singular Spectrum Analysis (MSSA) reconstruction and its application to volumes of receivers functions. More precisely, reconstruction tests applied to regional data acquired by the USArray in the Yellowstone region enable us to explore the regional variations of seismic discontinuities below receivers.

Our study suggests the presence of conversions from the 410-km, 520-km, and 660-km transition zone phase boundaries in addition to a double-phase 660-km precursor with strong negative polarity at a depth range of 580-km to 610-km. Amassed ancient oceanic material, a subducting slab, plume remnants, partial melt, and an increase in water content may be associated with the signals from these mid-transition zone conversions. Altogether, results obtained in this work reveal that multidimensional signal processing via MSSA assists data preconditioning and their subsequent mapping for identifying mantle transition zone interfaces.

*To my grandfathers, Juan Martínez (1945-2018) and Alfredo Bustinzar (1933-2019)*

# Acknowledgements

I want to recognize my supervisor Dr. Mauricio Sacchi for his full support and guidance from the very beginning. I am especially grateful for his patience, trust and genuine interest in the well-being of the group. Thank you for the many invaluable academic, professional and life lessons; this has been a memorable adventure for me.

I would also like to thank my co-supervisor, Dr. Yu Jeffrey Gu, for his continuous assistance and knowledgeable insights during the time of research. Thank you for your direction in reporting and presenting our work, as this would not have been possible without your supervision.

Special appreciation to the members of my examining committee for their time to evaluate and improve this thesis.

Thank you, colleagues and friends, from the Signal Analysis and Imaging Group (SAIG), and the Global Seismology Group for the numerous scientific discussions and your constructive criticism. I also wish to acknowledge Dr. Jinkun Cheng and Dr. Ramin Dokht for providing the indispensable codes and programs that made this work possible. Lastly, I want to thank Dr. Yunfeng Chen for being a mentor throughout this study and providing all the necessary tools. The waveforms used in this study were made accessible by the facilities of IRIS Data Services and, specifically, the IRIS Data Management Center.

Thank you to my friends Andrés Ambros, Breno Bahia, Fernanda Carozzi, Wenlei Gao, Gian Matharu, Iliana Papathanasaki, Min Ju Park and Kristian

Torres, who made this a gratifying experience. I also want to express a special appreciation to my friends Gregg Hansen, Edmund Jung, Vinayagah Nadasan, Wilber Liang, Diman Patel and Arman Sohi for making my experience in Edmonton more special than I could have ever imagined. I truly appreciate your kindness and company.

Last but certainly not least, I dedicate this work to my loving parents and beautiful sister, who never left my side and whose unconditional support made this accomplishment a reality. I will forever be in debt with you.

# Contents

<b>Abstract</b>	<b>ii</b>
<b>Acknowledgements</b>	<b>v</b>
<b>1 Introduction</b>	<b>1</b>
1.1 The Big Picture . . . . .	1
1.1.1 Earth's mantle overview . . . . .	1
1.1.2 The receiver function method . . . . .	3
1.1.3 Reconstruction of seismic data . . . . .	6
1.1.4 Noise attenuation . . . . .	7
1.2 Literature review . . . . .	7
1.2.1 Reconstruction methods for exploration seismology . . . . .	8
1.2.2 Reconstruction methods for Global Seismology . . . . .	16
1.3 Contribution . . . . .	18
1.4 Thesis Outline . . . . .	20

<b>2</b>	<b>Tensor representation of receiver functions</b>	<b>23</b>
2.1	Introduction . . . . .	23
2.2	Application . . . . .	26
2.3	Discussion . . . . .	30
<b>3</b>	<b>3D reconstruction of receiver functions</b>	<b>31</b>
3.1	Introduction . . . . .	31
3.2	Method . . . . .	34
3.2.1	2D SSA denoising . . . . .	34
3.2.2	3D MSSA denosing . . . . .	40
3.2.3	Reconstruction with a reinsertion algorithm . . . . .	41
3.3	Application . . . . .	43
3.3.1	Synthetic data . . . . .	43
3.3.2	Real data . . . . .	45
3.4	Discussion . . . . .	47
<b>4</b>	<b>5D reconstruction of receiver functions</b>	<b>54</b>
4.1	Introduction . . . . .	54
4.2	Method . . . . .	57
4.2.1	5D reconstruction . . . . .	57
4.2.2	Interpolation with a reinsertion algorithm . . . . .	62
4.3	Application . . . . .	62
4.3.1	Synthetic data . . . . .	62
4.3.2	Real data . . . . .	64
4.4	Discussion . . . . .	68

<b>5 Conclusion</b>	<b>76</b>
5.1 Summary . . . . .	76
5.2 Contributions and limitations . . . . .	80
5.3 Future work . . . . .	82
 <b>Bibliography</b>	 <b>84</b>

# List of Figures

1.1	Ray paths for converted waves . . . . .	4
1.2	Conversion of P-waves to S-waves . . . . .	5
2.1	A single source and receiver pair that demonstrates the spatial variable dependency of receiver functions. The station with latitude-longitude coordinates $(r_{x_0}, r_{y_0})$ records the event at a distance $\Delta_0$ and a back-azimuth $\phi_0$ relative to the receiver. . .	25
2.3	(a) A CRG (the green triangle) containing the events (the orange irregular polygons) sorted by common distance $\Delta$ and variable back-azimuth $\phi$ . (b) Common back-azimuth $\phi$ sorting with variable offset $\Delta$ . The sources are projected onto the surface to illustrate the sorting. . . . .	29
2.2	(a) Schematic representation of a grid of equidistant CRGs (common-receiver gathers) represented by the receiver in green. (b) Tensor representation of the multi-dimensional array storing the RFs. . . . .	29

3.1	Interpolation and denoising of synthetic 3D volumes composed of radial P receiver functions generated from a 1D velocity model. The x-axis and y-axis represent the theoretical back-azimuth sector of the events and the arrival time from P, respectively. The line at the top of each sector indicates the increasing epicentral distance. (a) Ideal synthetic volume representing three discontinuities. (b) The ideal synthetics after randomly removing 70% of the traces and an SNR of 0.5. (c) The recovered data from (b) after keeping the four largest eigenvalues. (d) The synthetics from (a) with an SNR of 2.0 and keeping 50% of the traces. (e) The output from (d) after keeping the largest five singular values. . . . .	49
3.2	Data for a fixed back-azimuth sector corresponding to $\phi = 180^\circ$ of the synthetics in Fig. 3.1, and the reconstruction quality for simulation with varying rank. (a,d) The input from Figs 3.1b and d. (b,e) The output from Figs 3.1c and e. The traces with peak amplitudes in both graphs are the original traces; the amplitudes of the missing traces increase with each reinsertion. (c,f) Keeping the four and five largest eigenvalues yields the highest quality of reconstruction for the synthetics in Figs 3.1b and d, respectively. . . . .	50
3.3	Selected stations survey acquisition geometry and statistics for 3D MSSA examples. (a,d,g) Summary stations with the center of the search radius being the new latitude and longitude station coordinates and equation (blue circles) 2.5 forms the summary common-receiver gather with a stacking weight of $P = 1/\mathbf{r}$ . The individual stations (in black) in their original location. (b,e,h) Back-azimuth distribution of the events illustrated using a linear scale with most events originating from the interval $0^\circ - 180^\circ$ . (c,f,i) Epicentral distance distribution for the events data set used to build a given summary station. The vertical axis represents the count. Although the distribution is approximately uniform, the count peaks for $\Delta > 70^\circ$ , which may contribute to the high levels of noise in the raw receiver functions. . . . .	51

3.4	Receiver function enhancement examples for the stations in Fig. 3.3 using equation 3.15. (a,c,e) The observed 3D data volume after binning along back-azimuth and epicentral distance prior to regularization. The first and fifth panels $\phi = 45^\circ$ and $\phi = 225^\circ$ show no distinguishable phases due to the high levels of incoherent noise and missing traces. (b,d,f) The filtered and interpolated data using the 3D proposed reinsertion algorithm implemented via the truncated SVD. . . . .	52
3.5	The time converted volumes for Fig. 3.4 and their corresponding stacked summary traces. (a,d,g) The output volumes after 3D MSSA in the depth domain with discontinuities located underneath the receivers. (b,e,h) The corresponding raw summary traces. (c,f,i) The summary traces after the recovery algorithm with discontinuity depths marked by the dark dashed-lines. . .	53
4.1	Reconstruction examples of 5D synthetic volumes from a 1D velocity structure. Single gathers from the receivers with indices ( $r_x = 4, r_y = 4$ ). (a,c) Corrupted data with 70% and 50% decimation, and an SNR of 0.5 and 2.0, respectively. (b,d) The corresponding output data after 5D MSSA using $k = 10$ . . . .	70
4.2	Back-azimuth slice at $\phi = 180^\circ$ for the single station gathers shown in Fig. 4.1, and the quality of reconstruction as a function of the rank of the Hankel matrix. (a,d) Figs 4.1b and d. (b,e) Figs 4.1c and e. (c,f) Choosing $k=8$ and $k=10$ produces the recovery quality for the synthetics in Figs 4.1b and d, respectively. An increase in spatial redundancy translates to an increase in dB for the recovered data sets for a fixed rank. That is, the volume depending on four spatial coordinates will be more robustly enhanced than the volume depending on three spatial variables, everything else constant. . . . .	71
4.3	Field acquisition geometry and statistics for 5D MSSA examples. (a) Irregular distribution of stations before binning in the Latitude-Longitude plane. (b) The overall distribution of the teleseismic events' distances. The vertical axis represents the count. (c) The overall distribution of the events' back-azimuths illustrated using a linear scale. . . . .	72

4.4	Regularly sampled data and fold, for the 5D examples. (a) Distribution of reconstructed summary stations in the regular grid. The black dots show their x-y coordinates and the blue circles correspond to a search radius of $r = 2^\circ$ . (b) The fold map of the 5D data structure showing the station density for a given cell. . . . .	73
4.5	Results of 5D real data set enhancement. The field data set is shown in 4.4. (a,d,g) The retrieved data illustrated by the latitude and longitude sector pairs $(r_x = 5, r_y = 4)$ , $(r_x = 5, r_y = 5)$ and $(r_x = 5, r_y = 6)$ , respectively. The RQRD implements the rank reduction step in the algorithm 4.6. (b,e,h) Time converted output volumes. (c,f,i) Stack of the enhanced depth-converted receiver functions with discontinuity depths (black dashed lines) and Pds arrivals. . . . .	74
4.6	Comparison of 3D and 5D reconstruction of seismic field data for the back-azimuth bin 6 ( $315^\circ - 45^\circ$ ) of the gathers in Fig. 3.4 and Fig. 4.5 using $\alpha = 0.4$ and $k = 10$ . (a,d,g) Input data. Slice for $\phi = 360^\circ$ . (b,e,h) The output data. Slice for $\phi = 360^\circ$ , the truncated SVD performs the rank reduction step. (c,f,i) The output data via fast 5D MSSA. Slice for $\phi = 360^\circ$ . The P410s and P660s waveforms are robustly enhanced, and a strong negative polarity P660s precursor waveform is observable across all panels at $60s - 70s$ . . . . .	75

---

---

# CHAPTER 1

---

## Introduction

### 1.1 Background

#### 1.1.1 The Earth's mantle

The Earth's mantle occupies a significant portion of the volume of the Earth. This bulk of mostly solid material remains below the crust, the thin outermost layer of the Earth, and above the hot and fluid outer core. Obtaining an accurate model of the density and seismic velocity structure of the mantle is crucial for grasping a more profound understanding of its past, present, and possibly future chemical composition and dynamical processes. Of particular interest is a subregion of the mantle denoted by sharp changes in the radial direction in the seismic structure as a result of changes in mineralogical phases and chemical composition (Birch, 1961; Ringwood, 1991).

Major seismic discontinuities observed globally at depths of 410 km and 660

km, on average, outline this subregion named the mantle transition zone or MTZ. Interestingly, there are some regions where discontinuities were reported at the depths of approximately 500 km, 520 km, and 560 km Gu et al. (1998), further subdividing the MTZ (Deuss and Woodhouse, 2001).

This subregion is characterized by a velocity gradient that is directly dependent on temperature. This dependency can explain the lateral variability in depths of the discontinuities (Helffrich and Bina, 1994). Ito and Katsura (1989) suggests that solid-state phase transitions of olivine is largely responsible for the temperature gradient and changes across the mantle transition zone or MTZ hereafter (Dziewonski and Anderson, 1981; Kennett et al., 1995).

Chemical differences can also influence observations of seismic discontinuities in the MTZ, in addition to the commonly accepted olivine phase transitions (Ita and Stixrude, 1992). The accumulation of oceanic material subducted under continental material is another factor that contributes to the structure of the mantle (Gu et al., 1998). All together, variations in iron and water content and the influences of pyroxene and garnet are attributable factors to the seismic structure of the MTZ.

In more recent decades, researchers have conducted many seismological investigations aiming to model, interpret, and prove the regional or global existence of these sharp boundaries along with their properties (Revenaugh and Jordan, 1991; Shearer and Masters, 1992; Shen et al., 2008; Deuss, 2009). The product of elastic parameters, compressional  $v_p$  and shear  $v_s$  velocities with density  $\rho$ , provides the impedance contrast along these seismic boundaries, which are

adequate indicators of topography, temperature and composition, and can be a direct interpretation of MTZ images. Likewise, changes in topography and elastic parameters along these seismic boundaries are effective indicators of local thermal and chemical properties.

### 1.1.2 Receiver function analysis

The receiver function method (RFM) (Langston, 1979; Ammon et al., 1990; Ammon, 1991; Cassidy, 1992; Gurrola et al., 1995; Ligorria and Ammon, 1999) is an important geophysical tool commonly employed to infer seismological observations beneath multi-component broadband stations, and it allows obtaining information over an extensive area in the order of a few hundred kilometres without having to probe the properties of the Earth directly. This technique has produced several complete studies of crustal (Langston, 1977; Owens et al., 1987; Owens and Crosson, 1988; Langston, 1989) and mantle structure (Owens, 1985; Dueker and Sheehan, 1997; Bostock, 1998; Farra and Vinnik, 2000; Lawrence and Shearer, 2006), and subduction zones (Langston, 1981; Owens et al., 1988; Li and Yuan, 2003). The RFM consists of the processing and interpretation of body waves that originate at teleseismic distances. Even though the Earth absorbs a considerable portion of the energy produced by an earthquake, a fraction of it is refracted by interior stratifications. The latter is recorded at the surface of the Earth by seismic station arrays like the USArray, J-Array, and Gräfenberg Array (Buttkus, 1986; Meltzer et al., 1999; Morita, 1996). Figure 1.1 illustrates this process. These waveforms contain

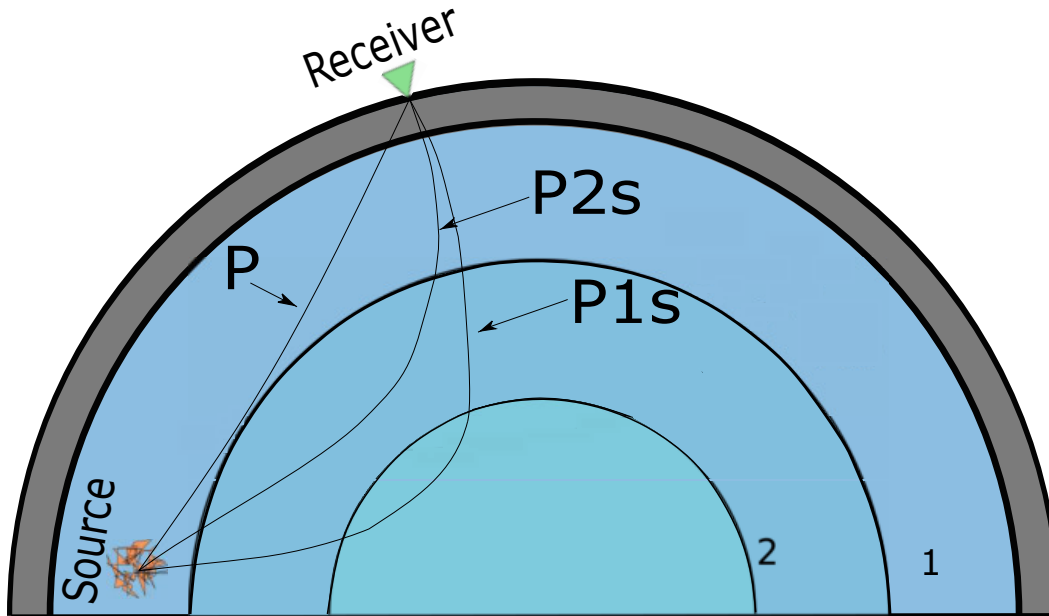


Figure 1.1: The approximate ray paths of the P wave and P-to-s conversions in a radially varying velocity structure with sharp changes at interfaces 1 and 2. The irregular polygon in orange represents the earthquake, and the triangle in green represents the receiver or seismic station. The teleseismic event interacts with interfaces 1 and 2 to produce the P1s, and P2s converted phases, respectively.

P-to-s converted phases, or Pds for short, where  $d$  denotes the depth to the interface. In a typical seismogram, one can distinguish several phases related to the depth of a discontinuity (Figure 1.2). Mathematically, a receiver function is a source-equalized time series that emerges from deconvolving the vertical from the horizontal impulse responses in the time domain, or by performing spectral division of the horizontal components by the vertical component. Moreover, it contains amplitude and timing information relative to the first arrival.

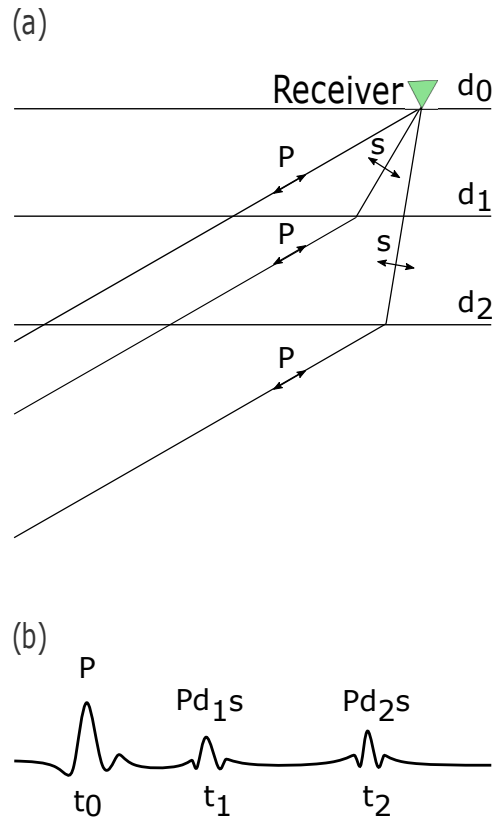


Figure 1.2: (a) Conversion of the up going P-waves to s-waves at depths  $d_1$  and  $d_2$ . The P-wave particle motion is parallel to the ray path, whereas the converted s-wave particle motion is perpendicular to the segments of the ray path between  $d_2-d_0$  and  $d_1-d_0$ . The receiver denoted by the green triangle records the P, Pd<sub>1</sub>s and Pd<sub>2</sub>s arrivals at the surface  $d_0$ . The ray samples the point where it switches polarity, so the waveform in (b) represents the footprint or measured wavefield approximately below the receiver. Because the ray emerges almost vertically at the surface, the horizontal component of the receiver measures the motion due to the s-wave only and some small part leaks into the vertical component.

### 1.1.3 Reconstruction of seismic data

Seismic methods adopted for exploration and global seismology use waves recorded by arrays of receivers to image the subsurface. In seismic exploration, human-made sources and arrays of receivers are optimally deployed on the surface of the Earth to illuminate the subregion beneath them. In general, sources and receivers cannot be deployed on regular grids due to the presence of obstacles, logistics and regulatory constraints. In the last two decades, applied seismologists have devoted significant efforts to multidimensional signal processing methods capable of reconstructing seismic surveys. In other words, acquired seismic data with irregular and insufficient source and receiver positions are processed via *seismic data reconstruction* algorithms to produce seismic volumes that are regularly sampled in source and receiver coordinates. Reconstruction methods are often based on Fourier inversion techniques (Liu and Sacchi, 2004; Xu et al., 2005; Abma and Kabir, 2006; Zwartjes and Sacchi, 2007; Trad, 2009) or rank-reduction techniques (Trickett et al., 2010; Oropeza and Sacchi, 2011; Gao et al., 2013a; Cheng et al., 2019; Carozzi and Sacchi, 2019). The main goal of reconstruction techniques is to simultaneously denoise and map seismic observations into a regular multidimensional grid. Reconstruction methods are prevalent in seismic exploration, but they have not received sufficient attention in global seismology yet. Global seismologists can decide on optimal coordinates of receiver stations, but they have no control on source (earthquake) coordinates. This research investigates numerical algorithms adopted by exploration seismologists and implements them for

preconditioning receiver functions.

### 1.1.4 Noise attenuation

Exploration seismologists have also been active in the development of multichannel signal enhancement techniques. Rather than attenuating noise by operating on one seismogram at the time, modern methods for seismic signal enhancement adopt multichannel signal processing where a group of seismograms is simultaneously processed to enhanced its signal-to-noise ratio. Nowadays, most common data processing algorithms exploit the coherence of signals across spatial coordinates such as receiver-source distance (Canales, 1984; Naghizadeh, 2012) or redundancy of information after transforming the data, for instance, via the normal moveout correction (Yilmaz, 2001). Similar ideas have been applied successfully in global seismology. For instance, Radon transforms originally developed in exploration seismology to isolate, and filter reflections have been adapted for preconditioning receivers function for the study of mantle discontinuities (An et al., 2007; Wilson and Guitton, 2007; Gu and Sacchi, 2009; Schultz and Gu, 2013; Aharchaou and Levander, 2016)

## 1.2 Literature review

In the past two decades, exploration seismologists have focused on regularization and denoising methods for seismic record enhancement. The enhancement or preconditioning of seismic records is a necessary step before imaging

via modern seismic migration algorithms (Trad, 2009). These algorithms require data that are sampled adequately in receiver and source coordinates. Regularization methods have also been adopted for Amplitude Versus Offset (AVO) and Amplitude Versus Azimuth (AVAz) compliant processing flows (Hunt et al., 2010). Access to dense and regularly sampled data for seismic migration and AVO inversion has been the main driver of research in the field of seismic reconstruction. In the next sections, I provide a literature review on data reconstruction techniques and their application to exploration and global seismology.

### **1.2.1 Reconstruction methods for exploration seismology**

Currently, seismic data restoration methods in the field of exploration seismology fall into one of the following categories:

- Transform-based methods
- Prediction error filtering techniques
- Methods based on rank-reduction techniques
- Methods that adopt principles of wave-propagation phenomena

## Transform-based reconstruction

A transform, in general, is a linear operator that permits to represent data in a new domain. For instance, data that depends on time ( $t$ ) can be represented in the frequency ( $\omega$ ) domain via the Fourier transform. Similarly, the Fourier transform can be used to map data that depends on time and space ( $t - x$ ) to the frequency wavenumber ( $\omega - k$ ) domain.

Numerical algorithms for data processing adopt discrete transforms such as the Discrete Fourier Transform, the Discrete Radon Transform, or the Discrete Curvelet Transform. These discrete transforms are used to represent a signal in the new domain in terms of coefficients. For instance, a two-dimensional signal in the  $t - x$  domain can be represented by Fourier coefficients in  $\omega - k$  space via the 2D Discrete Fourier Transform. The representation of a signal in a new domain is a simple task for regularly sampled data. For irregularly sampled data or data with missing observations, inversion techniques are required to estimate the coefficients that represent the data in the new domain (Sacchi et al., 1998). The estimated coefficients are utilized to synthesize data at new spatial positions. Transform-based reconstruction methods can be grouped into several subcategories. Below, I review the principal techniques proposed by the seismic exploration community.

### *Fourier Methods*

In this category of methods, the available data are mapped to the Fourier domain via iterative inversion, and then the new data are synthesized from the transformed domain. For instance, Sacchi et al. (1998) use the Discrete

Fourier Transform coefficients (DFT) to estimate Fourier coefficients from irregularly sampled data. The estimated Fourier coefficients via inversion are used to synthesize regularly sampled data. Many researchers have provided algorithms that use this principle. For instance, Zwartjes and Sacchi (2007) proposed an inversion procedure for estimating Fourier coefficients from irregularly sampled data where the sought coefficients are sparse. The technique of Zwartjes and Sacchi (2007) is often called Fourier Reconstruction via Sparse Inversion (FRSI). Similarly, Liu and Sacchi (2004) propose an algorithm where a weighted quadratic norm constrains the Fourier coefficients. The latter is called Minimum Weighted Norm Interpolation, a method profusely adopted for industrial applications such as prestack data reconstruction for generating amplitude compliant AVO and AVAz gathers (Sacchi and Liu, 2005; Downton et al., 2008; Hunt et al., 2010).

Another category of Fourier reconstruction methods is composed of iterative algorithms that apply amplitude thresholding in the  $\omega - k$  domain. An example of the latter is Projection onto Convex Sets (POCS) reconstruction, a technique introduced to the seismic processing community by Abma and Kabir (2006). It is interesting to mention that earlier work on POCS reconstruction of 2D geophysical maps is described in Menke (1991). POCS has also been adopted beyond reconstruction by Gao et al. (2013b) and for compressive reconstruction by Jiang et al. (2017).

Greedy algorithms have also been used to retrieve the Fourier coefficients that describe seismic observations. For instance, the Anti leakage Fourier Transform (ALFT) was proposed for multidimensional seismic data reconstruction

by Xu et al. (2005) and Xu et al. (2010). The method has also been adopted for 5D prestack reconstruction by Whiteside et al. (2014) and Ghaderpour et al. (2018). Another greedy method is Matching Pursuit Fourier interpolation (Ozbek et al., 2009) which has similarities to ALFT.

### *Radon methods*

The Radon transform (Darche, 1990; Sacchi and Ulrych, 1995; Trad et al., 2003) represents seismic observations in the  $\tau$ - $p$  domain ( $\tau$ - $p$ ) where one can perform filtering and then use an inverse  $\tau$ - $p$  transform to generate filtered data. The Radon transform can also be used for data reconstruction (Wang et al., 2010; Liu et al., 2013). In this case, data are first transformed to the Radon domain via inversion, and then the Radon domain coefficients are used to synthesize data at desired spatial positions. Radon reconstruction is considered an effective interpolation and reconstruction method for 2D datasets, but, in general, Radon methods are rarely adopted for multidimensional spatial reconstruction.

### *Curvelet Transform reconstruction*

The Curvelet Transform (Candès et al., 2005) is a local directional transformation of the data in terms of coefficients that described dip (orientation), scale (frequency content), and location. Similar to Fourier reconstruction methods, the Curvelet domain coefficients that model seismic observations are estimated via inversion methods. In general, sparsity-promoting inversion algorithms estimate the Curvelet coefficients (Herrmann and Hennenfent, 2008). Once the coefficients are estimated, they can be used to synthesize data at regular spa-

tial coordinates. In general, Curvelet reconstruction methods yield optimal results when the data that one wishes to reconstruct are randomly sampled (Herrmann et al., 2008; Hennenfent and Herrmann, 2008). Naghizadeh and Sacchi (2010a) further improve the Curvelet transform reconstruction method by developing an algorithm capable of reconstructing regularly data.

### **Prediction Error Filtering techniques**

Spatial Prediction Error Filters (Canales, 1984; Abma and Claerbout, 1995) have been proposed for random noise attenuation of seismic records. This technique assumes that seismic waveforms are predictable in the spatial domain, and linear prediction theory is adopted to estimate filters that are capable of modeling seismic reflections. The difference between the observed data and the modelled data is the additive random noise. This principle was adopted not only for noise attenuation but also for seismic data interpolation by Spitz (1991). The original algorithm proposed by Spitz (1991) permits to reconstruct 2D data, in other words, data that depend on time and one spatial dimension. Reconstruction methods based on Prediction Error Filtering have also been adopted for multidimensional seismic data reconstruction (Naghizadeh and Sacchi, 2007, 2008, 2010b).

### **Rank-reduction methods**

The principle of reconstruction of seismic data via reduced-rank methods can be simply stated as follows. The ideal data can be represented by matrices or

tensors (multi-linear arrays) that are low rank. Missing data and noise will increase the rank of these matrices or tensors in which one has embedded the observations. Then iterative rank-reduction methods can be used to recover the ideal and complete data. This principle is also used in the field of collaborative filtering for designing recommendation systems such as those used in e-commerce to recommend movies, books, etc (Herlocker et al., 2004; Sacchi et al., 2015).

*Methods that embed seismic data on Hankel matrices and block Hankel matrices*

In this category, available seismic observations are embedded into Hankel or block Hankel matrices. Under ideal conditions, these matrices are considered low-rank matrices. Iterative rank-reduction methods are adopted to estimate the missing observations and to improve the overall signal-to-noise ratio of the recorded seismic records.

This class of signal enhancement approach assumes that seismic data acquired under ideal conditions can be embedded into low-rank matrices. These methods take advantage of the spatial coherence and predictability of seismic data, in other words, the linear dependency of seismic observation between channels. The goal is to find an approximation of the observed data that is of lower rank by decomposing the data into coherent and incoherent parts (Freire and Ulrych, 1988). After reconstruction, the output data should be comparable to the data that one could have acquired under ideal conditions. An early method in this category is called Eigenimage filtering (Trickett, 2003) where rank-reduction is directly applied to spatial two-dimensional data at a given

frequency components. The truncated SVD is applied to reduce the rank of the measurements at a given temporal frequency by keeping the most significant singular values. This technique is often adopted to denoise cubes of data in the  $f - x - y$  (frequency and two spatial variables) domain.

A similar method to the Eigenimage Filtering technique was proposed for noise suppression and trace interpolation. This method differs in an extra step that organizes spatial data of a fixed temporal frequency into matrices with unique structures such as Toeplitz and Hankel matrices as a means to improve the coherency of the signal by increasing the redundancy in the measurements. This method, called Singular Spectrum Analysis (SSA) filtering (Vautard et al., 1992; Sacchi et al., 2009), owes its origin to the study of time series stemming from dynamical systems (Broomhead and King, 1986). The SSA method has also been called Cadzow filtering (Cadzow, 1988; Trickett, 2008), and the Caterpillar method (Nekrutkin, 1996; Stepanov and Golyandina, 2005). All these techniques are equivalent in the sense that they lead to similar algorithms and outputs, but were developed independently from separate fields. For instance, Cadzow filtering acts as a general framework for enhancing signals and images, whereas the Caterpillar method arises from the analysis of time series. Furthermore, Trickett et al. (2010) proposed a so-called hybrid method that simultaneously employs Eigenimage and Cadzow filtering along different spatial dimensions in an attempt to process data in all dimensions simultaneously.

The generalization of SSA for multiple dimensions, Multichannel Singular Spectrum analysis (MSSA) , is the method that will be used in this thesis

for preconditioning receiver functions. The need for rank reduction algorithms that act on several or all spatial variables at once was palpable and motivated the series of significant advances that efficiently deal with higher dimensional data (Oropeza and Sacchi, 2011; Gao et al., 2013a; Cheng et al., 2019; Carozzi and Sacchi, 2019).

*Methods that embed seismic data on tensors (multi-linear arrays)*

This category also performs rank reduction in the  $f - \mathbf{x}$  domain and assumes the data can be embedded in low-rank multilinear arrays also called tensors. A higher-order tensor represents the spatial data at a fixed temporal frequency. Then, the higher-order singular value decomposition reduces the rank of the higher-order tensor to suppress noise and estimate the missing observations.

Unlike methods that operate on Hankel and Block-Hankel matrices, this approach directly operates on the higher-order seismic tensor, rather than arranging the coefficients of the multidimensional spatial data in matrices with a unique structure. Tensor algebra is an ever-evolving mathematical tool that aims to complete missing data, and there is a significant amount of research done in various fields such as biomedical signal processing, social network analysis and computer vision (Acar and Yener, 2009).

Tensor seismic data reconstruction assumes that the fully sampled noise-free seismic data can be embedded in a tensor. The intention is to apply a higher-order singular value decomposition (HOSVD) to represent the data via low-rank tensor model. One can interpret the HOSVD decomposition as a generalization of the traditional SVD of matrices applied to tensors (Kreimer and

Sacchi, 2012). An extension or generalization of this method solves the seismic reconstruction problem via a constrained inversion that adopts nuclear norm regularization (Kreimer et al., 2013).

### **Methods that use principles of wave-propagation phenomena**

Wave equation principles provide reliable algorithms for seismic data restoration. The latter often employ physical models such as the Born approximation (Miranda, 2005) or Green's theorem (Ramírez and Weglein, 2009). Wave-equation principles provide a reliable way to seismic data enhancement by assuming a linear relationship between the data and an ideal zero-offset section (Ronen, 1987; Ramírez et al., 2006). Inversion methods can give an estimate of the subsurface model from the available data, and then data at new spatial positions can be generated via forward modelling. Wave equation based techniques allow the use of subsurface information such as a smooth macro-velocity model.

### **1.2.2 Reconstruction methods for Global Seismology data**

Although there has been recent work on techniques proposed to recover seismic data in the global seismology community, the number of passive-studies for large-scale networks of arrays that deal with higher dimensional data falls short compared with the amount research conducted by the exploration seismology community. Nonetheless, the studies mentioned below represent continuous efforts in paving the way towards reconstructing the wavefield recorded by

large seismic arrays. A significant roadblock in the journey towards the reconstruction of earthquake records stored in multidimensional arrays is that only structurally simple data can be recovered, such as P-to-s converted waves and reflections.

Some studies recover the wavefield beneath arrays of receivers through straightforward schemes such as sample-by-sample weighted stacking. For instance, Chai et al. (2015) applies a station-centred linearly decreasing weight to equalize the lateral sampling of receiver functions. Similarly, Neal and Pavlis (1999) and Song et al. (2017) use Gaussian weights to compute stacks at pseudo station locations within an arbitrary grid of receivers. Cubic spline functions are also apt for recovering samples across space (Sheldrake et al., 2002; Zhang and Zheng, 2014). This type of spatial smoothing wavefield recovery allows estimating the response at regular points within the location of interest, but in general, they tend to produce overly smooth results.

The Radon transform also provides a viable route for signal preconditioning (Wilson and Guitton, 2007; Gu and Sacchi, 2009). The Radon transform decomposes the recorded observations into coefficients in the  $\tau - p$  domain; an inverse transform yields the interpolated teleseismic data. The Curvelet or directional wave packets transform act as *flat* plane waves, providing a localized transform in the  $t - x$  domain for unwanted signal suppression by separating phases with differing slowness and similar to the Radon transform, an inverse transformation recovers the desired wavefield (Yu et al., 2017). Furthermore, Ventosa and Romanowicz (2015) developed the so-called Slant-Stacklet Transform by harnessing the power of the directional wavelet and slant-stack,

or Radon transforms to obtain cleaner reflections from the deep interior of the Earth. Sparse representation of signals on another domain also allows signal restoration; for instance, Schneider et al. (2017) use a POCS algorithm (Abma and Kabir, 2006) combined with the sparsity of signals in the  $f - k$  domain to enhance weak phase arrivals. Another example is the reconstruction of the surface wavefield proposed by Zhan et al. (2018) where they assume that the observed signal has a sparse representation in the wavenumber domain, at individual frequencies. More recently, Hu et al. (2018) present an exploration-based method that models seismograms at different receivers through coefficients that denote the stretching-and-squeezing in the time axis relative to one another. In the past decade, the application of rank-reduction methods has been on the rise given their capability for reconstructing multi-dimensional data from large arrays. However, recent investigations have only applied rank-reduction techniques to teleseismic data that depend on two spatial dimensions, at most (Gu et al., 2015; Dokht et al., 2016; Chen et al., 2019).

### 1.3 Contributions of this thesis

My thesis is concerned with geophysical signal processing and pays particular attention to the development of a strategy to reconstruct receiver functions and, consequently, improve the interpretability of mantle discontinuing. The following are specific contributions to my field of study.

- I first provide an overview of MSSA. Then I examine the application of the MSSA method on radial P-wave receiver functions as a proof of concept to simultaneously suppress incoherent noise and interpolate missing seismograms. Receiver functions in the past were generally processed on single, isolated stations, whereas spatial redundancy across a grid of broadband receivers is the basic premise of multichannel rank reduction methods. MSSA based processing can exploit spatial coherency to obtain more robust receiver functions estimates than single, isolated receiver processing and conventional reconstruction methods employed in the field of global seismology. I also aim to recover first order back-azimuthal and ray parameter variations across a less-than-ideal sampled network of receiver arrays like the USArray.
- A significant technical challenge lies in the selection of binning parameters required for the construction of the multidimensional arrays of receivers function that are processed via MSSA. A strategy to assemble these multidimensional gathers is also provided in this thesis.
- Recent work on data reconstruction via rank-reduction methods in the field of global seismology focused on common-receiver gathers (CRG) containing 2D volumes of data (Dokht et al., 2016), as well as wavefield reconstruction of a single event or common-source gather (CSG) (Chen et al., 2019). In this thesis, I present for the first time an application of the regularization of 3D and 5D volumes of receivers functions. To this end, I adopted binning techniques to produce large 3D volumes of single

station receiver functions that depend on time, distance and azimuth. The later allows running reconstruction preserving azimuth information, a key difference compared with the work of Dokht et al. (2016). Then, I also introduce multiple stations and multiple sources (earthquakes) to assemble a volume that depends on four spatial attributes and time. This strategy gives rise to a 5D data volume similar to those generally adopted in modern exploration seismology. To this date, no other author has proposed adopting 5D reconstruction to global seismic observations, which I affirm it is a substantial contribution as it paves the way for translating sophisticated modern signal enhancement methods to the processing of data acquired by seismic networks.

- Last, I stress that this thesis is mainly concerned with seismic data processing and its applications to receiver functions. However, it is essential to point out that the methodology developed in this work has permitted to analyze USArray data in the Yellowstone region and to explore regional variations of mantle discontinuities below receivers.

## 1.4 Thesis Outline

**Chapter 2** begins by introducing the spatial dependency of receiver functions and presents a new procedure to represent 3D CRGs sorted by back-azimuth and epicentral distance as well as 5D volumes containing a grid of CRGs by further considering the x-y coordinates of the stations. This procedure is based on the regular sampling requirement of the MSSA method and serves

as an initial step to alleviate spatial irregularities and sparse coverage and increase the signal-to-noise ratio of our data. This multidimensional data representation provides an insightful way to inspect back-azimuthal and offset variations across different stations. The designed binned spatial data geometry has the flexibility to be adjusted to simulate large networks of arrays such as the USArray.

**Chapter 3** presents a brief overview of the more straightforward 2D case of the SSA technique and expands the method to two spatial variables (MSSA). We employ the truncated SVD as the rank reduction step to enhance waveforms of P-to-S converted waves contained in 3D summary CRGs. This approach operates on synthetic gathers with different levels of decimation and random noise. To explore the performance on field data, we examine observations from the USArray, which provide an approximately dense, uniform sampling of the seismic wavefield beneath the grid of receivers located near the Yellowstone area.

**Chapter 4** expands MSSA to higher dimensions and introduces a computationally efficient rank reduction algorithm to reconstruct a collection of CRGs simultaneously. We test the performance of the proposed recovery algorithm on 5D synthetic and field data from the USArray in the Yellowstone area. We implement the low-rank constraint via the randomized QR decomposition. The suggested approach can recover a smooth version of the timing and amplitude of the receiver functions and is less strict on the rank selection than the truncated SVD.

**Chapter 5** contains a summary of key results and observations obtained throughout this research. I also identify limitations and present recommendations for future work and applications.

---

---

## CHAPTER 2

---

# Receiver functions represented as multi-dimensional arrays

### 2.1 Introduction

Passive source studies commonly use the RFM for seismological imaging purposes. Receiver functions are time series  $s(t)$  derived from multicomponent receiver recordings and computed by deconvolving the horizontal components by the vertical component to obtain an estimate of the reflectivity of the subsurface (Langston, 1979; Ligorria and Ammon, 1999). The amplitude and timing of the receiver functions depend on the ray parameter of the arrival (Gurrola et al., 1994), which is a direct consequence of the relative distance from the receiver to the epicentre of the event. For an inhomogeneous medium, the receiver function  $s(t, \Delta_0, \phi_0)$  represents the measurements made by the station from an event at a distance  $\Delta_0$  and a back-azimuth of  $\phi_0$ . To incorporate

the dependency on the path structure, we redefine the receiver function as  $s(t, r_{x_0}, r_{y_0}, \Delta_0, \phi_0)$  from the event at location  $(\Delta_0, \phi_0)$  measured by the receiver with coordinates  $(r_{x_0}, r_{y_0})$  as illustrated in Fig. 2.1.

Receiver function studies typically followed station-by-station processing as opposed to array-based processing, which can exploit the spatial redundancy in the measured wavefield. The demand for seismic arrays around the globe triggered an increase in broadband seismic arrays deployed in many countries, for instance, the USArray. Relatively uniformly spaced, dense networks of seismic arrays provide a more robust spatial sampling and are ideal for multi-channel based processing methods, such as MSSA. Furthermore, these grids of receivers provide useful ways to sort and store earthquake data. Gathers can sort a collection of seismic traces or receiver functions with a geometric attribute in common predicated on their path structure. For instance, offset, azimuth, midpoint, conversion point, depth point and angle of incidence are some of the many geometrical seismic attributes that provide distinct ways to gather the data. Moreover, gathers allow seismologists to perform quality control, frequency analysis and inspect for spatial variations within acquired data sets.

Seismologists have used various gathers to process receiver functions. A single station recording many events is called a common-receiver gather (CRG) (Dokht et al., 2016), and these can be further subdivided based on the spatial properties of the source, as we will discuss in the next section. Similarly, Chen et al. (2019) use a common-shot or common-source gather (CSG) to examine a single event recorded on a grid of receivers. A common-conversion point

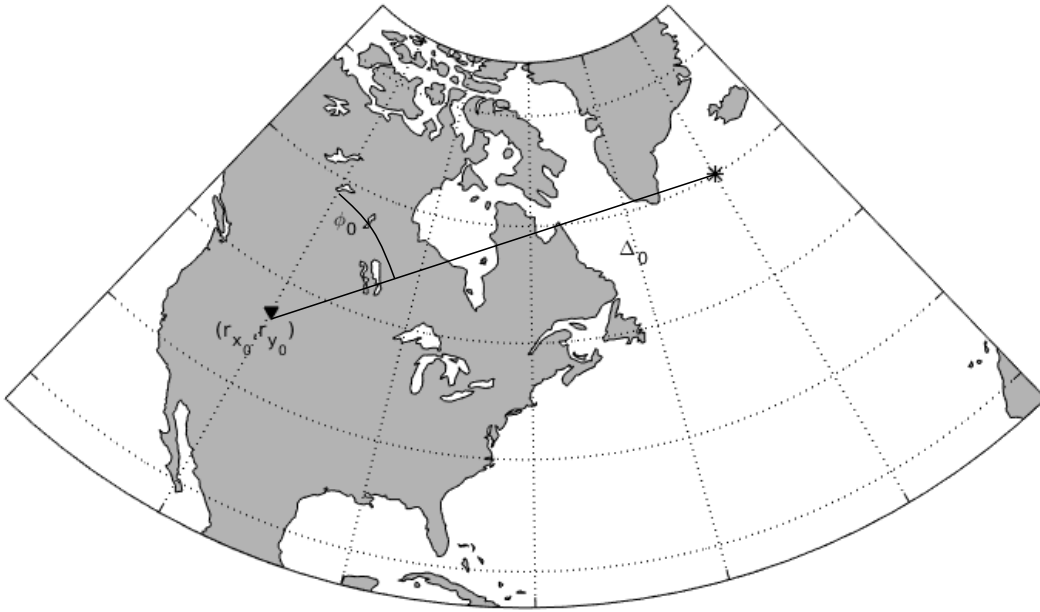


Figure 2.1: A single source and receiver pair that demonstrates the spatial variable dependency of receiver functions. The station with latitude-longitude coordinates  $(r_{x_0}, r_{y_0})$  records the event at a distance  $\Delta_0$  and a back-azimuth  $\phi_0$  relative to the receiver.

gather (CCPG) is a more sophisticated sorting problem that combines traces from multiple sources and receivers while accounting for the geometry of the Earth (Frassetto et al., 2010). A CCPG is analogous to a common-depth point gather (CDPG) from reflection seismology and a reference Earth model is typically needed to assemble these types of gathers.

In the next section, we define a regularly spaced areal grid of pseudo-CRGs that acts as a multi-channel or array-based framework in which to store and reconstruct receiver functions.

## 2.2 Method

Tensors can be particularly useful to represent seismic data recorded on a grid of receivers or stations such as the USArray. Given the receiver function's path structure dependencies, it is natural to represent seismic data in the station-event domain where  $(r_{x_0}, r_{y_0})$  indicates the station's location and  $(\Delta_0, \phi_0)$  the event's location.

We further define a field data acquisition survey. Singular spectrum analysis requires equidistant sampling in space (Sacchi et al., 2009), which motivates the following regular grid geometry (Carozzi and Sacchi, 2019):

$$r_x = r_{x_0}^{min} + \delta r_x (i_1 - 1), \quad i_1 = 1, \dots, nr_x. \quad (2.1)$$

$$r_y = r_{y_0}^{min} + \delta r_y (i_2 - 1), \quad i_2 = 1, \dots, nr_y. \quad (2.2)$$

$$\phi = \phi_0^{min} + \delta \phi (i_3 - 1), \quad i_3 = 1, \dots, n\phi. \quad (2.3)$$

$$\Delta = \Delta_0^{min} + \delta \Delta (i_4 - 1), \quad i_4 = 1, \dots, n\Delta. \quad (2.4)$$

We define above the centres of the bins where the indices  $(i_1, i_2, i_3, i_4)$  belong to the coordinates  $(r_x, r_y, \Delta, \phi)$ . The total number of stations is  $nr_x \times nr_y$  and the total number of distances and back-azimuths are  $n\Delta$  and  $n\phi$ , respectively. We assign the trace or RF with coordinates  $(r_{x_0}, r_{y_0}, \Delta_0, \phi_0)$  to the center of the closest bin with coordinates  $(r_x, r_y, \Delta, \phi)$ . Each center is bounded and  $s(t, r_{x_0}, r_{y_0}, \Delta_0, \phi_0)$  is assigned to  $d(t, r_x, r_y, \Delta, \phi)$  if there exists a trace in that

bin, otherwise a zero trace is assigned to represent the missing observation. We avoid notation clutter by letting  $\mathbf{r}_0 = (r_{x_0}, r_{y_0})$ ,  $\mathbf{s}_0 = (\Delta_0, \phi_0)$ ,  $\mathbf{r} = (r_x, r_y)$  and  $\mathbf{s} = (\Delta, \phi)$  such that  $s(t, r_{x_0}, r_{y_0}, \Delta_0, \phi_0) = s(t, \mathbf{r}_0, \mathbf{s}_0)$  and  $d(t, r_x, r_y, \Delta, \phi) = d(t, \mathbf{r}, \mathbf{s})$ .

The aforementioned method of assigning an observed trace to a regularly sampled structure is often called 'binning' in Exploration Geophysics (Onajite, 2014). The binning process is extended to deal with traces and stations populating the same center by introducing an inverse-distance weighting (IDW) to each RF (Shepard, 1968).

$$d(t, \mathbf{r}, \mathbf{s}) = \frac{\sum_{q=1}^Q s_q(t, \mathbf{r}_0, \mathbf{s}_0) w_q(\mathbf{r}, \mathbf{s})}{\sum_{q=1}^Q w_q(\mathbf{r}, \mathbf{s})} \quad (2.5)$$

such that,

$$\Delta_0 \in [\Delta - \delta\Delta, \Delta + \delta\Delta] \quad (2.6)$$

$$\phi_0 \in [\phi - \delta\phi, \phi + \delta\phi] \quad (2.7)$$

$$\mathbf{r}_0 \leq r \quad (2.8)$$

where,

$$w_q(\mathbf{r}, \mathbf{s}) = \frac{1}{(\|\mathbf{r} - \mathbf{r}_{0q}\| \|\mathbf{s} - \mathbf{s}_{0q}\|)^P}. \quad (2.9)$$

In this formulation,  $Q$  is the total number of traces contained in the bin with indices  $(i_1, i_2, i_3, i_4)$ ,  $r$  is the radius enclosing  $(r_x, r_y)$  and  $P$  is a positive real number that assigns a higher weight to receiver functions closest to the bin.

The parameter  $P$  is analogous to the degree of smoothing and the extent to which distant observations influence the resulting stacked receiver function. We repeat this process for adjacent overlapping bins, thereby creating a moving average with IDW that assembles a tensor  $d(t, i_1, i_2, i_3, i_4)$  containing all the RFs for a given set of stations, distances and back-azimuths. The process of binning is not a necessity for synthetic data as discretization can ensure regular sampling. However, real data benefits from this process since measurements have continuous representation and irregular sampling in space. Additionally, this work-flow serves the following two purposes:

- (1). Increases signal coherency (SNR). Particularly useful for weak and noisy secondary conversions as it is often the case for RFs.
- (2). Decrease the number of empty sectors or missing observations from areas with low coverage and data sets composed of a relatively small number of events.

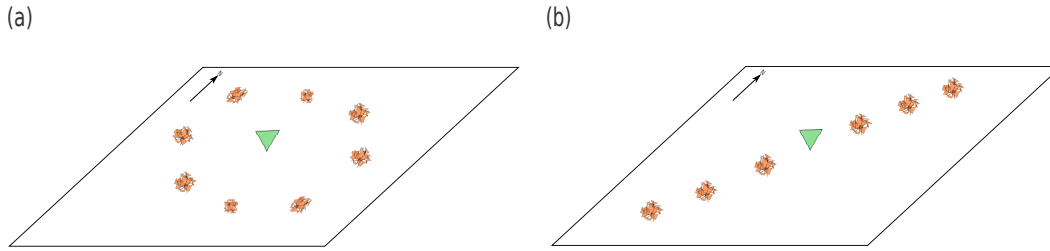


Figure 2.3: (a) A CRG (the green triangle) containing the events (the orange irregular polygons) sorted by common distance  $\Delta$  and variable back-azimuth  $\phi$ . (b) Common back-azimuth  $\phi$  sorting with variable offset  $\Delta$ . The sources are projected onto the surface to illustrate the sorting.

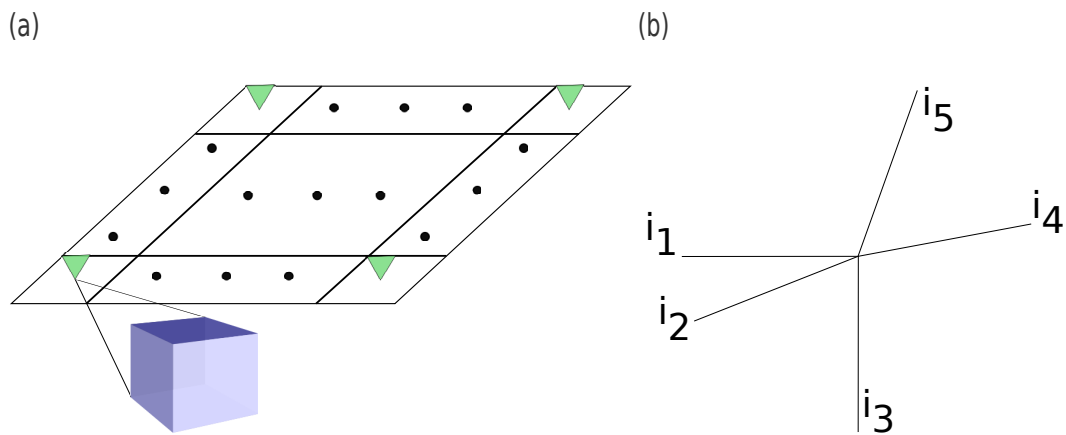


Figure 2.2: (a) Schematic representation of a grid of equidistant CRGs (common-receiver gathers) represented by the receiver in green. (b) Tensor representation of the multi-dimensional array storing the RFs.

## 2.3 Discussion

In this chapter, we present an alternative approach to representing RFs that incorporates their spatial and path structure dependencies. Their spatial features and geometrical properties allow forming unique domains for viewing and sorting these time series. The multi-dimensional arrays presented in this chapter allow MSSA to reconstruct the RFs based on the signal redundancy and coherency contained in the gathers due to the sources' geometric patterns. The assembly of the seismic data arrays can be tailored to mimic a particular network of seismic arrays by varying the binning parameters. Furthermore, this approach provides control over the degree of spatial smoothing or averaging of the stacked traces, which in turn dictates the order of the preserved seismic features.

Our binning process is straightforward. It considers a smaller region within the whole data set and creates equally spaced pseudo-CRGs, and further sorts them in the back-azimuth-distance space based on an IDW scheme. The binning process places equal importance on the pseudo-CRGs and further subdomains, accounting for differences in the number of observations at each node. The method presented is capable of overcoming the shortcomings inherent in single station RF analysis and provides an explicitly multi-channel framework in which to represent and process receiver functions.

---

---

## CHAPTER 3

---

### 3D reconstruction of receiver functions

#### 3.1 Introduction

SSA (Singular Spectrum Analysis) is a non-parametric method, and as such, it does not rely on assumptions about the data, making it compatible with stationary and non-stationary time series (Hassani et al., 2013). Informally, the technique decomposes the observations into its components so they can be classified as signal or noise and improves it by discarding the undesired elements (Hassani et al., 2007).

Researchers across many disciplines have proved SSA fruitful time after time as a signal processing and time series analysis tool. Vautard et al. (1992) provide a comprehensive review of the theoretical and algorithmic characteristics of SSA for short, noisy, chaotic signals from a signal processing point of view. Kondrashov et al. (2010) adopted SSA to fill gaps in the solar wind and interplanetary magnetic field data to promote model simulation and validation by

providing time-continuous data sets. In medicine, Sanei et al. (2011) propose an adaptive SSA technique to distinguish heart sound from murmur, which is a result of various heart abnormalities. More recently, the fields of economics and finance have also investigated its potential in multiple areas (Hassani and Thomakos, 2010). Thomakos et al. (2002) decompose modelled futures volatility series to capture the market trends and periodicities to aid in options pricing and risk management. Hassani et al. (2010) investigate the impact of noise attenuation in financial series and its effect on the measures of linear and nonlinear dependencies of financial data. Leles et al. (2018) propose two separate versions of singular spectrum analysis to design a trend-following trading scheme. Lahmiri (2018) uses SSA in conjunction with support vector regression and particle swarm optimization for intraday stock price prediction. Strictly speaking, SSA acts on a single channel or variable and deals with time series that vary with time. However, in the context of seismology, SSA operates on data sets with two dimensions, the second being some coordinate in space. We assume that the underlying signal also varies in space, allowing for a frequency by frequency application of SSA along with the various measurements in space. Hence, the rank reduction of 2D data sets needs a 1D approach. More specifically, the treatment of 2D seismic data is termed SSA because it acts on a single spatial variable.

In this chapter, we extend the attenuation of noise that is dissimilar from trace to trace and the recovery of laterally continuous signals from two-dimensional seismic records and three-dimensional records. Given that SSA works on a single frequency at once, this requires a two-dimensional MSSA (Multi-channel

Singular Spectrum Analysis), which acts on two independent spatial coordinates simultaneously. Read (1993) first developed the treatment multi-variate or multi-channel analysis by forming a frequency-dependent trajectory matrix containing information from all channels. The expansion to multiple dimensions has a significant improvement in the quality of the recovered data.

There are four steps in the reconstruction workflow presented in this chapter. The first step forms a Hankel-structure trajectory matrix composed of lagged vectors from the entries of a given temporal frequency. Next, the assembled matrix undergoes factorization using the SVD. The decomposed matrix is then rank-reduced by discarding singular values past a specified threshold. As the last step, anti-diagonal averaging of the rank-reduced matrix recovers the seismic signal.

This chapter presents the basic theory behind SSA, focusing on its application for reconstructing receiver functions. We begin by introducing a simple case where the data depend on two variables (one temporal and one spatial variable). Then we followed with the more general instance with the addition of a second spatial variable and thus, expanding to multi-variate or multi-channel SSA (MSSA). This work quantifies the results of this approach on 3D synthetic data using the quality of reconstruction factor. We evaluate its performance on real 3D data by filling gaps in the records and robustly enhancing mantle transition zone conversions.

## 3.2 Theory

### 3.2.1 2D Singular Spectrum Analysis (SSA) denoising

We begin our discussion of Singular Spectrum Analysis (SSA) by introducing the signal model as a function of a single spatial variable. Traditionally, SSA is considered a non-parameter approach because it was designed independently of any particular signal model. However, we will show that SSA is particularly tailored to analyze signals that are composed of a superposition of complex exponentials. We first propose to analyze data, more specifically, a window of data, that is composed of a unique linear event or a waveform with constant dip or ray parameter  $p$  in the  $t - x$  domain. Such a signal can be represented in  $t - x$  as  $d(t, x) = w(t - px,)$  where  $w(t)$  is the source function or wavelet. This simple signal can be mapped to the  $f - x$  domain by taking the Fourier transform.

$$d(t, x) = w(t - px) \Leftrightarrow D(\omega, x) = W(\omega)e^{-i\omega px}, \quad (3.1)$$

where  $W(\omega)$  denotes the Fourier transform of  $w(t)$ . For a series of  $nx$  equally spaced traces, the discrete spatial variable becomes  $x_n = (n - 1)\Delta x$ ,  $n = 1 \dots nx$  where  $\Delta x$  is the distance between adjacent receivers. We could rewrite equation 3.1 as follows,

$$D_n(\omega) = W(\omega) e^{-i\omega(n-1)p\Delta x}, \quad n = 1, 2, \dots, nx. \quad (3.2)$$

It is clear from equation 3.2 that the seismic signal can be represented via a complex exponential in  $f-x$  space. To avoid notational clutter, we can ignore the dependency on  $\omega$  but bear in mind that the described process must be carried out for all components in the seismic frequency band  $\omega \in [\omega_{min}, \omega_{max}]$ . After simplifying the notation we express equation 3.2 via

$$D_n = A e^{-i\alpha n} \quad n = 1, 2, \dots, nx, \quad (3.3)$$

where  $A = W e^{i\omega p \Delta x}$  and  $\alpha = \omega p \Delta x$ . It is easy to show that last expression can be written in a recursive form

$$D_n = a D_{n-1} \quad (3.4)$$

where  $a$  is a complex coefficient. We define the vector of observations via the following  $\mathbf{D} = (D_1, D_2, D_3, \dots, D_{nx})^T$  and the Hankel or Trajectory matrix associated to it (Sacchi et al., 2009)

$$\mathbf{H} = \mathcal{H}(\mathbf{D}) = \begin{pmatrix} D_1 & D_2 & D_3 & \dots & D_{lx} \\ D_2 & D_3 & D_4 & \dots & D_{lx+1} \\ D_3 & D_4 & D_5 & \dots & D_{lx+1} \\ \vdots & \vdots & \vdots & \ddots & \vdots \\ D_{mx} & D_{mx+1} & D_{mx+2} & \dots & D_{nx} \end{pmatrix} \quad (3.5)$$

We call the operator  $\mathcal{H}(\cdot)$ , the Hankelization operator. The Hankel matrix is a particular structure in which each anti-diagonal is constant. One can also define an operator that maps back the Hankel matrix  $\mathbf{H}$  into the data and we will call this operator the anti-diagonal averaging operator  $\mathcal{A}$  which

$$\mathcal{A}(\mathbf{H}) = \mathbf{D} \quad (3.6)$$

$$= (D_1, D_2, D_3, \dots, D_{nx})^T. \quad (3.7)$$

The size of  $\mathbf{H}$  is  $(mx \times lx)$  and is chosen such that  $mx = \lfloor \frac{nx}{2} \rfloor + 1$  and  $lx = nx - mx + 1$ . With this selection of  $mx$  and  $lx$ ,  $\mathbf{H}$  is a square or almost square matrix and  $mx \leq nx$ . As demonstrated, for consecutive spatial measurements, the recursive relation  $D_n = aD_{n-1}$  naturally models our signal. One can now express the columns of  $\mathbf{H}$  as linear combinations of each other. By using equation 3.4, it is easy to show that the Hankel matrix is given by

$$\mathbf{H} = \begin{pmatrix} D_1 & aD_1 & a^2D_1 & \dots & a^{lx-1}D_1 \\ D_2 & aD_2 & a^2D_2 & \dots & a^{lx-1}D_2 \\ \vdots & \vdots & \vdots & \ddots & \vdots \\ D_{mx} & aD_{mx} & a^2D_{mx} & \dots & a^{lx-1}D_{mx} \end{pmatrix}. \quad (3.8)$$

It is clear from the above expression that equation 3.8 is a rank-one matrix ( $\text{rank}(\mathbf{H}) = 1$ ). One can prove that for data that consist of  $k$  dipoles,  $\text{rank}(\mathbf{H}) = k$ . It is worth noting when noise or missing observation corrupt the data, the rank of the Hankel matrix increases. Therefore, one can use rank reduction methods as means of noise attenuation and signal reconstruction.

The truncated Singular Value Decomposition (SVD) (Andrews and Patterson, 1975; Golub and Van Loan, 1996) can be used to find the low-rank approximation of the trajectory matrix in equation 3.5 (Eckart and Young, 1936; Hansen, 1987). The SVD decomposition of the matrix  $\mathbf{H}$ , which can approximate any matrix by one of lower rank, is given by

$$\mathbf{H} = \mathbf{U}\mathbf{\Sigma}\mathbf{U}^\dagger \quad (3.9)$$

where  $\mathbf{U}$  and  $\mathbf{V}$  are unitary matrices and  $\mathbf{\Sigma}$  is a diagonal matrix. The symbol  $\dagger$  indicates the conjugate transpose. The size of the matrix  $\mathbf{U}$  is  $(mx \times lx)$  whereas the size of the matrix  $\mathbf{V}$  is  $(lx \times lx)$ . The matrix  $\mathbf{\Sigma}$  is the  $(lx \times lx)$  diagonal matrix of singular values sorted in descending order  $\sigma_1 \geq \sigma_2 \geq \sigma_3 \geq \dots \sigma_{lx}$ . The columns of the matrices  $\mathbf{U}$  and  $\mathbf{V}$  are the eigenvectors of outer  $\mathbf{H}\mathbf{H}^\dagger$  and inner  $\mathbf{H}^\dagger\mathbf{H}$  products, respectively. Similarly, the singular vectors  $\sigma_i$

are related to the eigenvalues  $\lambda_i$  of  $\mathbf{H}\mathbf{H}^\dagger$  and  $\mathbf{H}^\dagger\mathbf{H}$  via  $\sigma_i^2 = \lambda_i$ . The Eckart and Young theorem (Eckart and Young, 1936) states that the matrix of rank  $k$ ,  $\mathbf{H}_k$  that minimize  $\|\mathbf{H} - \mathbf{H}_k\|_F$  is given by <sup>1</sup>

$$\begin{aligned} \mathbf{H}_k &= \mathcal{R}(\mathbf{H}) \\ &= \mathbf{U}_k \mathbf{\Sigma}_k \mathbf{V}_k^\dagger, \end{aligned} \tag{3.10}$$

where  $\mathbf{U}_k$  and  $\mathbf{V}_k$  are matrices with the first  $k$  columns of  $\mathbf{U}$  and  $\mathbf{V}$ , respectively. Similarly,  $\mathbf{\Sigma}_k$  is the  $(k \times k)$  diagonal matrix with the largest  $k$  singular values of  $\mathbf{\Sigma}$ . The operator  $\mathcal{R}(\cdot)$  is a compact notation for rank reduction that will become useful in the development of the SSA filter. The SVD approximation can also be written as follows:

$$\begin{aligned} \mathbf{H}_k &= \mathcal{R}(\mathbf{H}) \\ &= \sum_{n=1}^k \sigma_n \mathbf{u}_n \mathbf{v}_n^\dagger \end{aligned} \tag{3.11}$$

which clearly shows that  $\mathbf{H}_k$  can be written as the superposition of rank-one matrices of the form  $\mathbf{u}_k \mathbf{v}_k^\dagger$ . This method is compelling for noise suppression since most of the coherent energy tends to map into the first few eigenimages allowing for the separation of signal from incoherent noise. Moreover, this procedure is equivalent to eigenimage filtering when the matrix to be rank-reduced is not a trajectory matrix but rather a frequency slice in the  $f - x - y$

---

<sup>1</sup> $\|\cdot\|_F$  denotes the Frobenius norm of a matrix.

domain (Trickett, 2003).

After obtaining the approximation of rank  $k$ ,  $\mathbf{H}_k$ , the denoised data is synthesized by averaging across the anti-diagonals of  $\mathbf{H}_k$  via the operator  $\mathcal{A}(\cdot)$  (Oropeza and Sacchi, 2011). We recall that we have designated  $\mathcal{R}(\cdot)$  the rank-reduction operator,  $\mathcal{H}(\cdot)$  the Hankelization operator then SSA filter can be expressed via the following expression

$$\hat{\mathbf{D}} = \mathcal{A}(\mathcal{R}(\mathcal{H}(\mathbf{D}))), \quad (3.12)$$

where  $\hat{\mathbf{D}}$  is the denoised data via SSA .

We can summarize SSA denosing as follows:

Transform to frequency domain  $d(t, x) \rightarrow D(\omega, x)$

For each frequency  $\omega$

Form spatial data vector  $\mathbf{D} = (D(\omega, 1), D(\omega, 2) \dots, D(\omega, nx))^T$

Form Hankel matrix  $\mathbf{H} = \mathcal{H}(\mathbf{D})$

Apply rank reduction  $\mathbf{H}_k = \mathcal{R}(\mathbf{H})$

Antidiagonal averaging  $\hat{\mathbf{D}} = \mathcal{A}(\mathbf{H}_k)$

End  $\omega$  loop

Transform back to time  $\hat{D}(\omega, x) \rightarrow \hat{d}(t, x)$

### 3.2.2 3D Multichannel Singular Spectrum Analysis (MSSA) denoising

We now adapt our analysis to data that depend on a temporal variable and two spatial variables; this implies that we extend SSA to MSSA. The temporal window can be mapped to the frequency domain  $d(t, x_1, x_2) \leftrightarrow D(\omega, x_1, x_2)$ . We consider the analysis for one frequency  $\omega$  and ignore dependency on frequency to simplify notation. If  $x_{1n} = (n - 1)\Delta x_1, n = 1, \dots, nx_1$  and  $x_{2n} = (n - 1)\Delta x_2, n = 1, \dots, nx_2$ . Then we can form a level-one Hankel matrix from every component of the first dimension

$$\mathbf{H}_{n_2}^{(1)} = \begin{pmatrix} D_{1,n_2} & D_{2,n_2} & \dots & D_{lx_1,n_2} \\ D_{2,n_2} & D_{3,n_2} & \dots & D_{lx_1+1,n_2} \\ \vdots & \vdots & \ddots & \vdots \\ D_{mx_1,n_2} & D_{mx_1+1,n_2} & \dots & D_{nx_1,n_2} \end{pmatrix} \quad (3.13)$$

Note that matrices in equation 3.13 are embedded in a level-two or block Hankel matrix, where each entry is a level-one Hankel matrix (Oropeza and Sacchi, 2011),

$$\mathbf{H}^{(2)} = \begin{pmatrix} \mathbf{H}_1^{(1)} & \mathbf{H}_2^{(1)} & \dots & \mathbf{H}_{lx_2}^{(1)} \\ \mathbf{H}_2^{(1)} & \mathbf{H}_3^{(1)} & \dots & \mathbf{H}_{lx_2+1}^{(1)} \\ \vdots & \vdots & \ddots & \vdots \\ \mathbf{H}_{mx_2}^{(1)} & \mathbf{H}_{mx_2+1}^{(1)} & \dots & \mathbf{H}_{nx_2}^{(1)} \end{pmatrix} \quad (3.14)$$

$\mathbf{H}^{(2)}$  is of size  $(mx_1 mx_2 \times lx_1 lx_2)$ , where  $mx_i = \lfloor \frac{nx_i}{2} \rfloor + 1$ ,  $lx_i = nx_i - mx_i + 1$  and  $i = 1, 2$ . MSSA is equivalent to SSA but, rather than operating on Hankel matrices, now the rank-reduction is applied to a block Hankel matrix. Similarly, we have to replace the antidiagonal averaging operator by the block antidiagonal averaging operator. Again, we filter the data via truncated SVD to compute  $\mathbf{H}_k^{(2)}$  and express the filtering process as

$$\hat{\mathbf{D}} = \mathcal{A}(\mathcal{R}(\mathcal{H}(\mathbf{D}))), \quad (3.15)$$

where now  $\mathbf{D}$  and  $\hat{\mathbf{D}}$  are data matrices for a single frequency  $\omega$ . It is worth noting that the filtering operator  $\mathcal{R}(\cdot)$  heavily depends on the application of an SVD, which can be slow and even infeasible for exceedingly large data sets. As an alternative, one can adopt a randomized singular value decomposition (R-SVD) to accelerate the algorithm (Liberty et al., 2007a; Rokhlin et al., 2009). We refer interested readers to Appendix A in (Oropeza and Sacchi, 2011). The following section introduces a new algorithm to alleviate the computational cost, which is necessary since the Hankel matrix to be rank-reduced can grow very large, very fast.

### 3.2.3 Data reconstruction with a reinsertion algorithm

The acquisition of earthquake data consists of measuring the displacement of the ground generated by the propagating wavefield beneath — receivers placed at discrete intervals on the surface of the Earth record the ground motion. Due to land, logistical and economic challenges, unavoidably, there

will be some irregularity on the receiver spacing. Consequently, there will be gaps in the data from irregular sampling. Missing observations arising from less-than-ideal acquisition conditions will also increase the rank of the matrix to be rank-reduced. Abma and Kabir (2006) proposed an algorithm to regularize the irregular sampled data. Their method consists of iteratively applying a threshold in the Fourier domain and replacing the recovered data in the original observations to recover the amplitudes of the missing records. We adopt an iterative algorithm presented in (Oropeza and Sacchi, 2011) rather than thresholding the frequency spectrum, we find a low-rank approximation using MSSA. The filtering and interpolation steps apply the MSSA operator to carry out both processes simultaneously

$$\begin{aligned} \mathbf{D}^0 &= \mathbf{D}^{obs} \\ \mathbf{D}^\nu &= \alpha \mathbf{D}^{obs} + (\mathbf{1} - \alpha \mathbf{S}) \circ \mathcal{F}(\mathbf{D}^{\nu-1}), \quad \nu = 1, 2, \dots, n_{iter} \end{aligned} \tag{3.16}$$

where  $\mathcal{F}(\cdot) = \mathcal{ARH}(\cdot)$  is the synthesis of the SSA or MSSA filter and where  $\mathbf{D}^{obs}$  is the array representing the observed data. The symbol  $\circ$  is element-wise product. The sampling operator  $\mathbf{S}(\cdot) \mathbf{S}$ , which has a value of 1 where a measurement exists and 0 otherwise. The scalar  $\alpha$  is the reinsertion weight and is related to the noise level. It represents the extent to which we honour the data. The symbol  $\mathbf{1}$  is an array of ones the same size as the observed data.

### 3.3 Results

In this section, we evaluate the performance of 3D reconstruction on several theoretical and field data sets containing P-to-s receiver functions from MTZ conversions. The MSSA operator  $\mathcal{F}(\cdot)$  works on  $n_\omega = 72$  frequency slices, where  $\omega \in [0.01, 0.36]Hz$  in each run for a total of  $n_{iter} = 150$  iterations by performing the truncated SVD. We adopt a reinsertion weight of  $\alpha = 0.4$  to honour the original observations robustly.

#### 3.3.1 Synthetic data

We generate synthetic P-to-s receiver functions from MTZ conversions using a matrix propagator approach (Dokht et al., 2016) for a homogeneous Earth with a 1D velocity structure (Dziewonski and Anderson, 1981). The generated data simulates three approximately linear events in the  $t - \Delta - \phi$  domain corresponding to the P220s, P410s and P660s phases, epicentral distances  $\Delta \in [45, 90]^\circ$  and a frequency band of  $\omega \in [0.1, 1.5]Hz$ . The temporal length of the window is 65s with a sampling interval of 0.1s. Lastly, we determine their theoretically optimal rank by quantifying the reconstruction quality of the output data in decibels (dB) as

$$Q(dB) = \frac{\|d(t, \mathbf{r}, \mathbf{s})\|_2^2}{\|d(t, \mathbf{r}, \mathbf{s}) - \hat{d}(t, \mathbf{r}, \mathbf{s})\|_2^2} \quad (3.17)$$

where  $d(t, \mathbf{r}, \mathbf{s})$  and  $\hat{d}(t, \mathbf{r}, \mathbf{s})$  represent the ideal and recovered data, respectively. With the choice of where  $n_t = 651$ ,  $n\Delta = 46$  and  $n\phi = 8$ , we construct a 3D CRG by repeating the synthetic matrix  $d(t, \Delta)$  along the additional spatial variable  $\phi$  for a set of eight evenly spaced back-azimuth sectors  $\phi \in [45, 360]^\circ$  to create  $d(t, \Delta, \phi)$ . Consequently, the noise-free, complete and ideally sampled data ( $Q_{in} = \infty$ ) in Fig. 3.1a is of size  $(n_t \times n\Delta \times n\phi)$ . The size of the block Hankel matrices for this example is  $(92 \times 120)$ . The panels are identical before decimation since we assume an azimuthally invariant 1D structure. This assumption will be sufficient to illustrate the capabilities of the suggested method.

Our procedure uses the sampling operator  $\mathbf{S}(\cdot)$  to randomly remove receiver functions from the volume. Also, we populate the data with random levels of incoherent noise to mimic gaps in data acquisition observed in the field. The previous step generates two input data sets. The first is 70% empty and has an SNR of 0.5, resulting in an input quality of  $Q_{in} = -1.1dB$  in Fig. 3.1b. Similarly, the second volume is 50% empty and has an SNR of 2.0, which corresponds to an input quality of  $Q_{in} = 1.1dB$  in Fig. 3.1d. The recovered data sets show output quality factors of  $Q_{out} = 6.60dB$  and  $Q_{out} = 8.80dB$ , respectively (Figs 3.2c and e). Our algorithm effectively recovers the coherent secondary conversions, multiples and reverberations while attenuating the noise.

We achieve maximal recovery using a rank of  $k = 4$  for the first data set, whereas  $k = 5$  is required to sufficiently recover the second data set (see Figs 3.2d and e). The ranks underscore the importance of the most significant

singular values in data recovery. Equally important, we observe a sharp increase in quality when preserving the first eigenvalues since they contain most of the coherent signal. In contrast, a systematic decrease occurs at higher ranks due to the overfitting of the noise.

### 3.3.2 Field data

In this section, we explore the effectiveness of 3D recovery on recordings from the USArray and map the seismic structure of the mantle transition zone beneath the receivers in the Yellowstone area. Despite the efforts in acquisition design, the sources and receivers still follow a non-ideal distribution. More precisely, although the USArray is programmed to follow a dense network of seismographs, its actual deployments introduce irregularities. Furthermore, there is no control over the timing and distribution of the sources relative to the array; this challenge further translates to incomplete measurements.

We restrict the investigation to events with ray parameters between  $0.08s/rad$  and  $0.04s/rad$ , which are typical of teleseismic events and are ideal for RF studies (Gurrola et al., 1994). First, to implement MSSA, we must ensure regular sampling of the input data. We bin the data following the geometry described by equations 2.1 to 2.4 and use equation 2.5 to construct the seismic volumes by stacking all the receiver functions populating a given bin. Hence, all the observations that satisfy equations 2.6 to 2.8. We then adopt the inverse distance weighting (IDW) stacking approach from equation 2.9 with a distance-dependent smoothing weight of  $P = 1$ . Like in the synthetic examples, the

sampling operator  $\mathbf{S}(\cdot)$  quantifies the degree of sparseness in the data after binning.

We apply some quality control on the data as an initial step and preprocess the data by applying a band-pass filter with corner frequencies  $f_c = [0.01, 0.03, 0.33, 0.36]Hz$  due to a decrease in recovery performance for higher frequencies. The procedure employs reconstruction parameters of  $alpha = 0.4$ ,  $n_{iter} = 150$ ,  $\omega \in [0.01, 0.36]Hz$ ,  $n_\omega = 72$  and a value of  $k = 10$  is chosen to follow the strategy of  $k \approx 2(k_{true})$  (Sacchi et al., 2009).

We test the reconstruction algorithm on three separate data sets. To do so, we build summary stations, or common-receiver gathers  $d(t, \Delta, \phi)$  sorted by epicentral distance and back-azimuth. Then, we construct the summary stations from 72, 84 and 85 individual stations containing a total of 3950, 4743 and 3961 receiver functions originally. The binning parameters are as follows:

- Summary station latitude-longitude coordinates:

$$\cdot \mathbf{r}_{i_1} = (-110.5, 43.5 + i_1 - 1)^\circ, i_1 = 1, 2, 3 \text{ and } r = 2^\circ$$

- Epicentral distance sectors for each summary station:

$$\cdot \Delta_{i_2} \in [\Delta_0^{min} - (2 - i_2)\delta\Delta, \Delta_0^{min} + (i_2)\delta\Delta], \Delta_0^{min} = 31^\circ, \delta\Delta = 1^\circ \text{ and } i_2 = 1, \dots, n\Delta = 59$$

- Back-azimuth sectors for each summary station:

$$\cdot \phi_{i_3} \in [\phi_0^{min} - (2 - i_3)\delta\phi, \phi_0^{min} + (i_3)\delta\phi], \phi_0^{min} = 45^\circ, \delta\phi = 45^\circ \text{ and } i_3 = 1, \dots, n\phi = 8$$

After regularizing the spatial distribution, we obtain three evenly spaced volumes with spatial dimensions of  $(n_t \times n\Delta \times n\phi)$  with  $n_t = 651$ ,  $n\Delta = 59$  and  $n\phi = 8$  and corresponding Hankel matrices of size  $(120 \times 150)$ . The gathers store a total of 393, 401 and 392 receiver functions and are equivalent to 17%, 15% and 17% decimation, respectively. Fig. 3.3 shows the initial positions of the stations from the USArray and the new position of their corresponding summary station.

The MSSA filter parameter is  $k = 10$  as it captures most of the information. Small rank  $k$  leads to very harsh denoising, which produces unrealistic solutions. On the other hand, larger values return noisier reconstructions. There are no easily identifiable phases in the input stacks with panels  $\phi = 45^\circ$  and  $\phi = 225^\circ$  due to the high levels of noise and zero traces (See Fig. 3.4), their corresponding time-to-depth converted representations and stacked summary trace in Fig. 3.5 and Fig. 3.4, respectively. In addition to the successful prediction of the arrival times and amplitudes of the interpolated receiver functions, the proposed method preserves the P410s, P520s and P660s phases. We also identify a robust negative polarity double phase preceding the P660s discontinuity.

### 3.4 Conclusion

In this chapter, we began by introducing singular spectrum analysis as a signal processing and time series analysis tool to enhance data by separating it into its constituents. We mentioned various applications of SSA reported in the

literature from many different fields and introduced it in the context of seismic data reconstruction. The development of SSA capable of handling two spatial variables was also covered, which was called MSSA. For this, a Hankelization operator arranges the elements of given monochromatic frequency into a level-2 Block Hankel matrix. Subsequently, a rank reduction and anti-diagonal operator act on the trajectory matrix to return an enhanced estimate of the seismic records. The POCS based reinsertion algorithm simultaneously filters and interpolates the receiver functions to estimate the amplitude of the recovered traces. We tested MSSA on corrupted synthetic seismograms containing theoretical conversions from the MTZ. We quantified the results by computing the reconstruction quality in dB. This chapter also includes several examples of 3D field data reconstruction and mapped the seismic structure below the pseudo-CRGs. The results presented in this chapter suggest that MSSA is an essential processing step to robustly enhance secondary conversions and fill gaps in the seismic records from irregularities in the acquisition step.

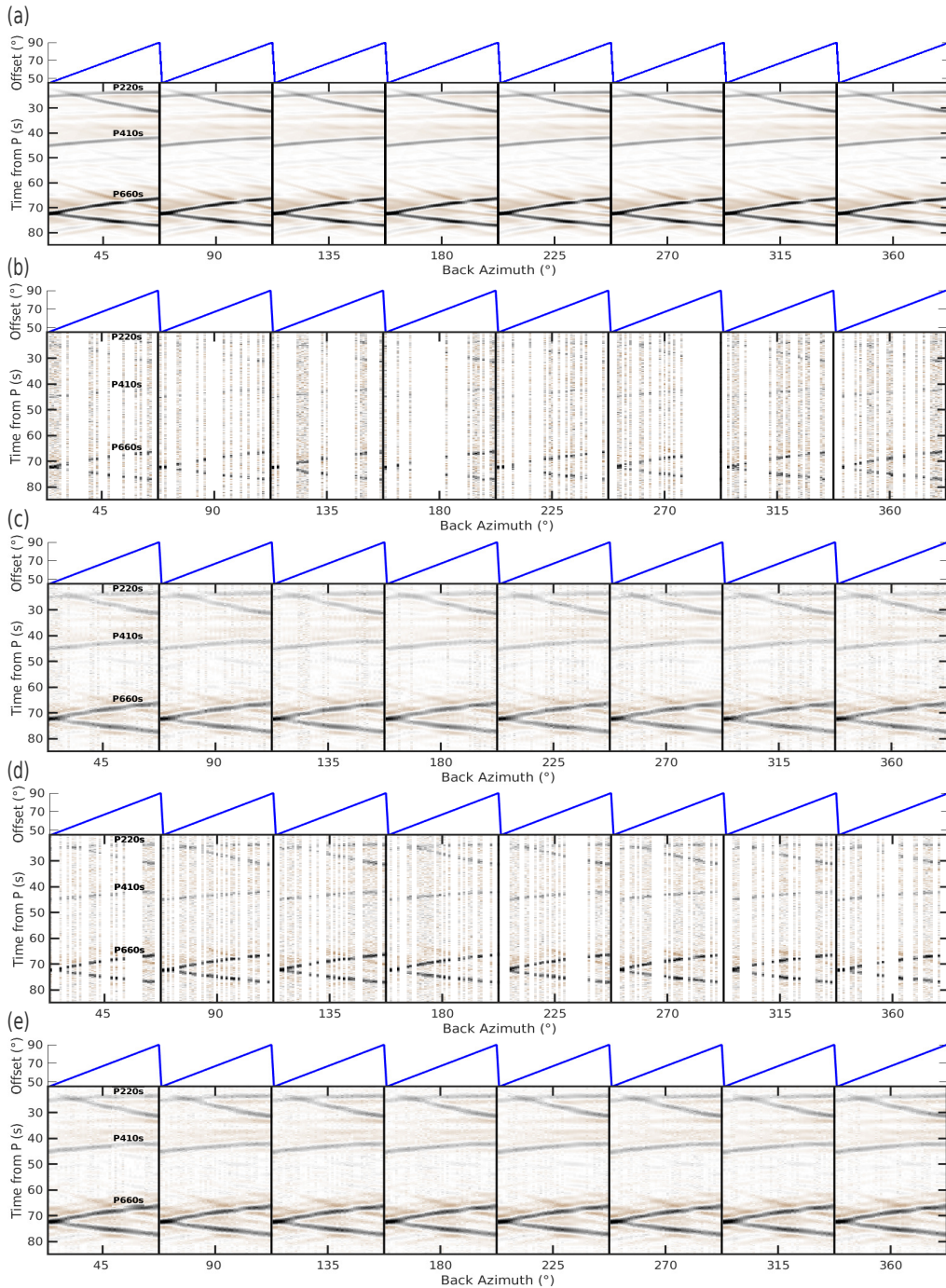


Figure 3.1: Interpolation and denoising of synthetic 3D volumes composed of radial P receiver functions generated from a 1D velocity model. The x-axis and y-axis represent the theoretical back-azimuth sector of the events and the arrival time from P, respectively. The line at the top of each sector indicates the increasing epicentral distance. (a) Ideal synthetic volume representing three discontinuities. (b) The ideal synthetics after randomly removing 70% of the traces and an SNR of 0.5. (c) The recovered data from (b) after keeping the four largest eigenvalues. (d) The synthetics from (a) with an SNR of 2.0 and keeping 50% of the traces. (e) The output from (d) after keeping the largest five singular values.

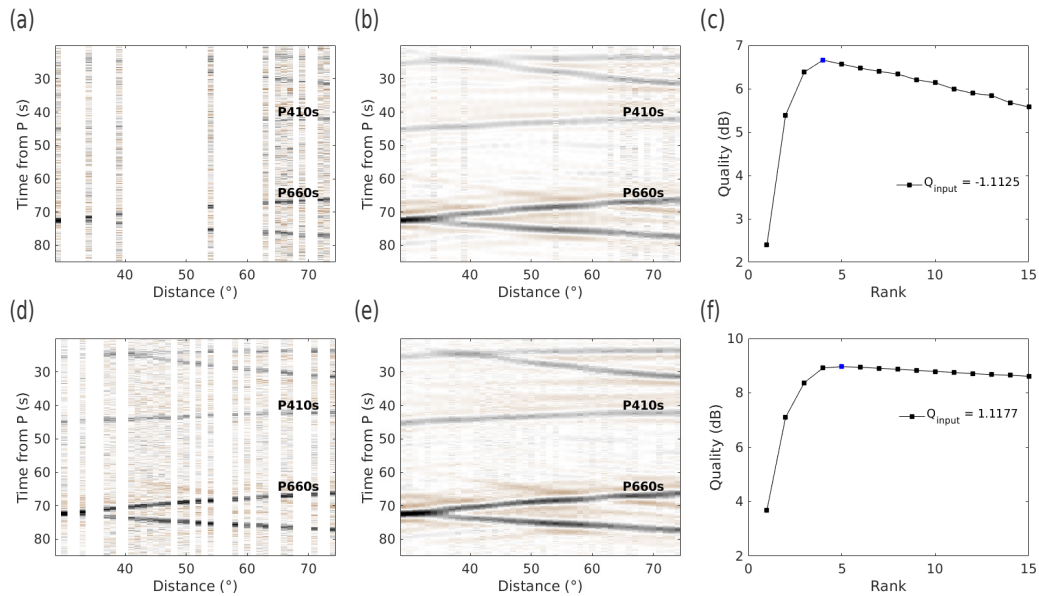


Figure 3.2: Data for a fixed back-azimuth sector corresponding to  $\phi = 180^\circ$  of the synthetics in Fig. 3.1, and the reconstruction quality for simulation with varying rank. (a,d) The input from Figs 3.1b and d. (b,e) The output from Figs 3.1c and e. The traces with peak amplitudes in both graphs are the original traces; the amplitudes of the missing traces increase with each reinsertion. (c,f) Keeping the four and five largest eigenvalues yields the highest quality of reconstruction for the synthetics in Figs 3.1b and d, respectively.

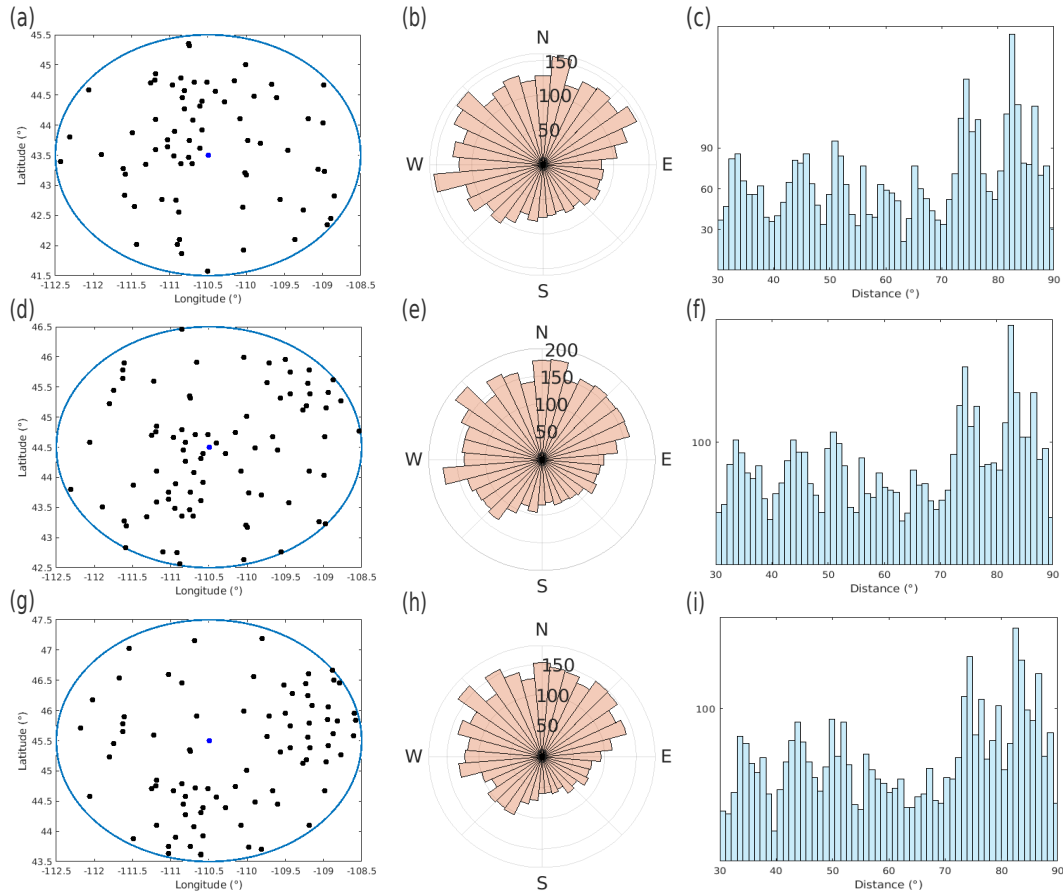


Figure 3.3: Selected stations survey acquisition geometry and statistics for 3D MSSA examples. (a,d,g) Summary stations with the center of the search radius being the new latitude and longitude station coordinates and equation (blue circles) 2.5 forms the summary common-receiver gather with a stacking weight of  $P = 1/r$ . The individual stations (in black) in their original location. (b,e,h) Back-azimuth distribution of the events illustrated using a linear scale with most events originating from the interval  $0^\circ - 180^\circ$ . (c,f,i) Epicentral distance distribution for the events data set used to build a given summary station. The vertical axis represents the count. Although the distribution is approximately uniform, the count peaks for  $\Delta > 70^\circ$ , which may contribute to the high levels of noise in the raw receiver functions.

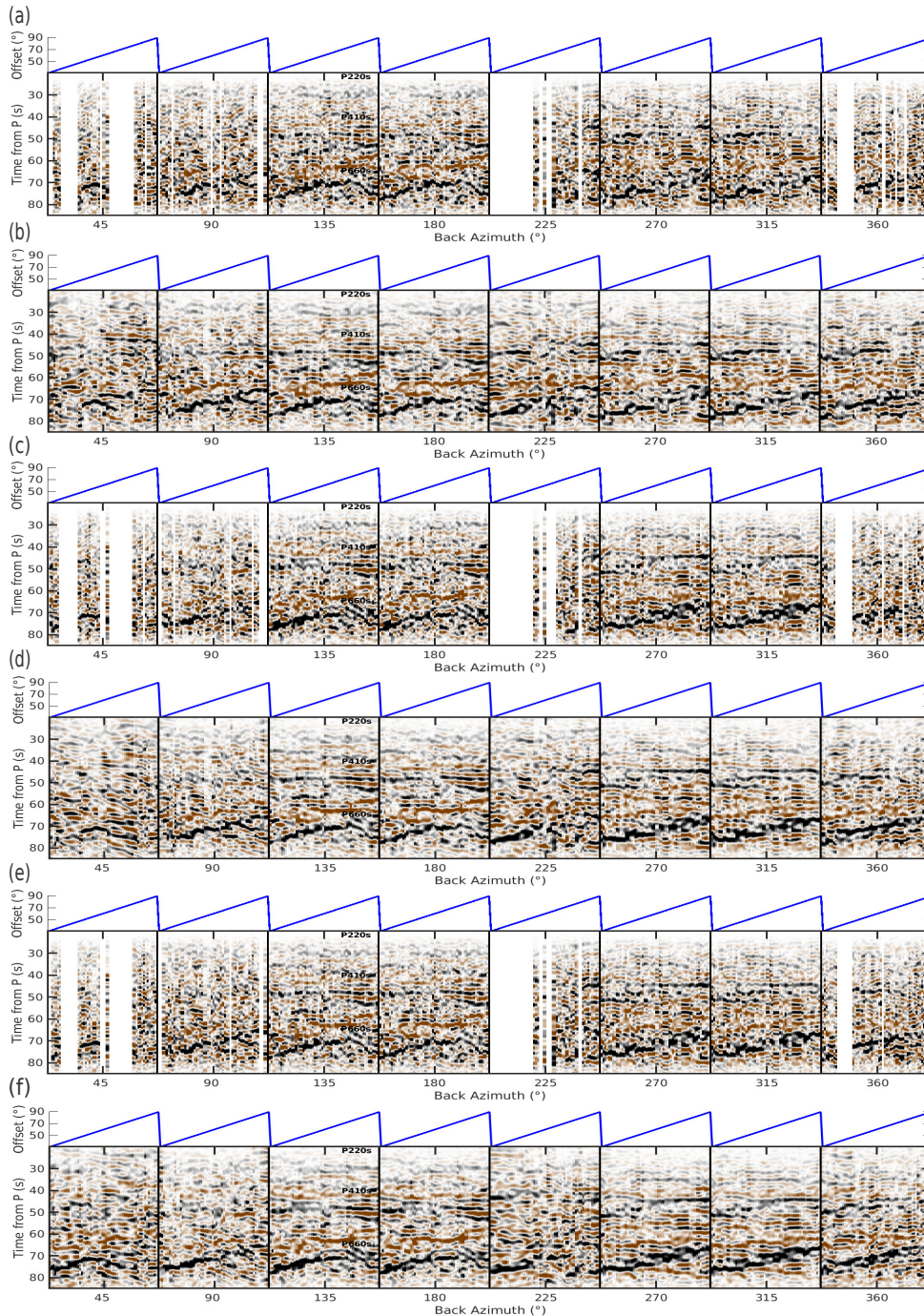


Figure 3.4: Receiver function enhancement examples for the stations in Fig. 3.3 using equation 3.15. (a,c,e) The observed 3D data volume after binning along back-azimuth and epicentral distance prior to regularization. The first and fifth panels  $\phi = 45^\circ$  and  $\phi = 225^\circ$  show no distinguishable phases due to the high levels of incoherent noise and missing traces. (b,d,f) The filtered and interpolated data using the 3D proposed reinsertion algorithm implemented via the truncated SVD.

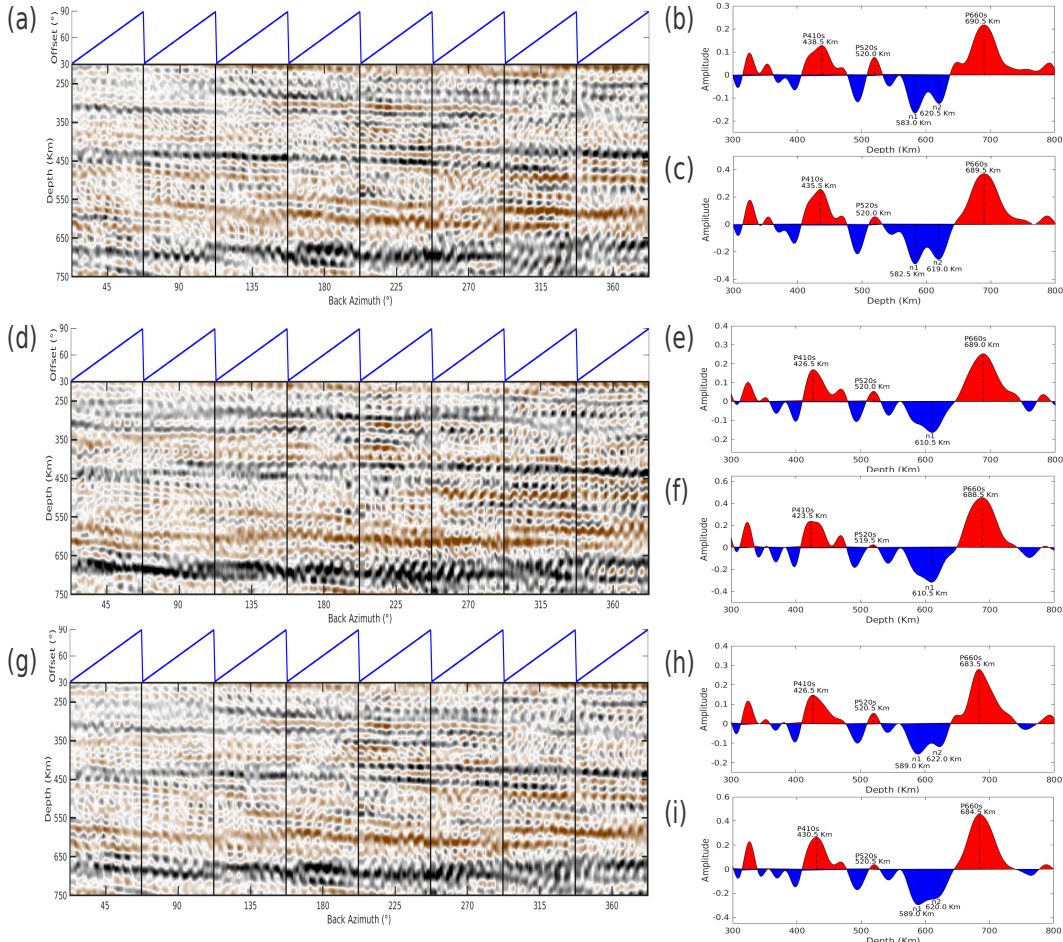


Figure 3.5: The time converted volumes for Fig. 3.4 and their corresponding stacked summary traces. (a,d,g) The output volumes after 3D MSSA in the depth domain with discontinuities located underneath the receivers. (b,e,h) The corresponding raw summary traces. (c,f,i) The summary traces after the recovery algorithm with discontinuity depths marked by the dark dashed-lines.

---

---

## CHAPTER 4

---

### 5D reconstruction of receiver functions

#### 4.1 Introduction

This chapter focuses on the generalization of SSA to the reconstruction of RFs arranged in a 5D tensor. The recovery algorithm acts on four spatial dimensions for all frequencies, and as such, it is considered a 4D MSSA. The previous chapter introduced the concept of denoising and interpolating 3D pseudo-CRGs containing RFs simultaneously. We capture offset and back-azimuth dependent features by representing earthquake records as 3D gathers. This type of representation is more familiar to the human mind as it is easy to visualize. However, it is also possible to process seismic data represented in 5D volumes by incorporating the x-y position of the receiver. To illustrate, we briefly present a link between seismic data dimensionality and singular spectrum analysis.

A 1D signal or a single receiver function will only vary with time since we

do not consider its spatial dependence. Consequently, SSA acts in the time domain by forming a trajectory matrix containing time samples. A 2D gather depending on time and a single space coordinate can also be enhanced using 1D SSA, but this process is carried out in the  $f - x$  domain by reorganizing spatial samples into a Hankel matrix. This treatment relies on the assumption that the signal model is predictable in space. Examples of 2D records are CSGs and CRGs that consider only one coordinate of the receivers or the sources, respectively. As we saw in the previous chapter, a 3D gather contains a second spatial variable and time. 2D MSSA is capable of enhancing these records in the  $f - xy$  domain by forming level-2 block Hankel matrices for each frequency. In chapter 2, we show that A 5D volume can represent events recorded on a grid or network of receivers. MSSA can analyze the information contained in all dimensions following the same steps described in Chapter 3. The reconstruction algorithm is identical regardless of the dimensionality of the seismic data, and the addition of more information may improve the results. However, the computational cost is much more substantial as the size of the trajectory matrix grows at a rapid pace with every added dimension. Consequently, this implies more memory to store the Level-four block Hankel matrix and higher computation power to perform rank-reduction using the SVD (Golub and Van Loan, 1996).

Many authors have examined rank reduction based reconstruction algorithms that attempt to alleviate the computational cost that comes with operating on higher-dimensional seismic data sets. For instance, Trickett (2003) suggests Lanczos bidiagonalization as a lower-cost alternative for decomposing the ma-

trices to be rank reduced and a hybrid between SVD and Lanczos as a more accurate approach. Furthermore, Gao et al. (2013a) present a method to decrease the computational demand of this decomposition by implementing fast matrix-vector multiplications using the fast Fourier transform. Other techniques involve a randomization stage in the MSSA algorithm. Oropeza and Sacchi (2011) randomize the SVD (R-SVD) to speed up the reconstruction by operating on a smaller randomized version of the trajectory matrix (Liberty et al., 2007b; Rokhlin et al., 2009). More recently, Cheng et al. (2019) implement a randomized version of pivoted QR factorization (RQRD) in conjunction with the fast matrix-vector multiplication method discussed by Gao et al. (2013a) to avoid explicitly building trajectory matrices and mitigate the computational complexity.

This chapter focuses on the generalization and adaptation of SSA to the reconstruction of earthquake data arranged in a 5D tensor. The computationally efficient recovery algorithm acts on four spatial dimensions for all frequencies, and as such, it is considered a 4D fast MSSA (FMSSA). We present synthetic and field data examples from the USArray that illustrate the ability of the algorithm to distinguish periodic from incoherent events, increase SNR and interpolate gaps in 5D receiver function records.

## 4.2 Theory

### 4.2.1 5D MSSA

We propose to adapt fast multi-channel singular spectrum analysis (FMSSA) to deliver a fast and memory-efficient version of MSSA (Cheng et al., 2019). This approach implements an economic decomposition through dimensionality reduction via random projections and exploits the structure of Hankel matrices to avoid explicitly constructing them without jeopardizing accuracy. Although the approach is intended for data that depend on four regularly sampled spatial variables  $D(\omega, x_1, x_2, x_3, x_4)$  where  $x_{i n_i} = (n_i - 1)\Delta x_i$  with  $n_i = 1, \dots, n x_i$  and  $i = 1, 2, 3, 4$ , we chose to provide a comprehensive and intuitive explanation of the method by illustrating with the simplest case, namely FSSA knowing that it can be generalized to 5D FMSSA without complications. We drop the dependency on  $\omega$  and perform the procedure over all the frequencies in the signal.

We implement the randomized QR decomposition (RQRD) as an alternative to the SVD in the rank-reduction step to the level-one Hankel matrix from equation 3.8 (Halko et al., 2011; Chiron et al., 2014; Cheng and Sacchi, 2016). As a first step, we reduce the dimensionality of the problem by performing a random projection on the Hankel matrix

$$\mathbf{G} = \mathbf{H}\Psi \tag{4.1}$$

We recall that traditional SSA requires forming and storing the Hankel structured  $(mx \times lx)$  matrix  $\mathbf{H}$ , where  $lx \leq mx$ . In contrast, the proposed algorithm in this section avoids that step. Here,  $\mathbf{\Psi}$  is a matrix of size  $(lx \times \kappa)$  which handles  $\kappa$  random linearly independent vectors and where  $\kappa \leq mx$ . Thus, the shrunk random projection has a size of  $(mx \times \kappa)$ . This technique transforms the data into a lower-dimensional space representation while maximizing the variance in the data. What is more, O’Leary and Simmons (1981), and Gao et al. (2013a) show that one can find an equivalent Toeplitz matrix representation of the data, embed it into a level-one circulant matrix and then apply an FFT to get the columns of 4.1. Although their algorithm works on Toeplitz matrices, both forms are tightly related, and one can go back and forth from both by reversing the order of their rows or columns. This simple transformation makes the proposed workflow plausible for Hankel matrices too and leads to the fast Toeplitz matrix-vector multiplication step, which is key in avoiding the construction of Hankel matrices

$$\mathbf{g}_i = \mathbf{H}\psi_i = \mathbf{T}\gamma_i, \quad i = 1, \dots, \kappa. \quad (4.2)$$

Where  $\mathbf{g}_i$  and  $\psi_i$  denote the the  $i$ th columns of  $\mathbf{G}$  and  $\mathbf{\Psi}$ , respectively. In parallel, reversing the order of  $\mathbf{G}$  and  $\psi_i$  yields  $\mathbf{T}$  and  $\gamma_i$ . Consequently,  $\mathbf{T}$  is a level-one Toeplitz matrix. The next step entails the multiplication of a  $(cx \times cx)$  circulant matrix  $\mathbf{C}$  defined below and an augmented vector padded

with zeros. Sacchi and Porsani (1999) demonstrates that an FFT efficiently computes this product.

$$\hat{\mathbf{g}}_i = \mathbf{C}\hat{\gamma}_i \equiv \mathcal{IFFT}(\mathcal{FFT}(\hat{\mathbf{c}}) \circ \mathcal{FFT}(\hat{\gamma}_i)), \quad i = 1, \dots, \kappa. \quad (4.3)$$

Where  $\mathcal{IFFT}(\cdot)$  and  $\mathcal{FFT}(\cdot)$  indicate the fast Fourier transform operator and its inverse,  $\hat{\mathbf{c}}$  is the first column of  $\mathbf{C}$ ,  $\circ$  indicates element-wise multiplication and  $\hat{\gamma}_i$  is  $\psi_i$  reversed and zero-padded to length  $cx$ , where  $cx = 2^J$ ,  $J \in \mathbb{Z}$

$$\hat{\mathbf{c}} = (D_{lx}, \dots, D_{cx}, D_1, D_2, \dots, D_{lx-1})^T \quad (4.4)$$

Finally, we retrieve the columns of the smaller matrix  $\mathbf{G}$  by extraction of the first  $mx$  elements of  $\hat{\mathbf{g}}_i$ . We emphasize the fact that the computation requires forming neither the Hankel nor the circulant matrix; we only need to save  $\hat{\mathbf{c}}$ . The complexity of the computation of the circulant matrix and augmented vectors products are in the order of  $\mathcal{O}(cx \log_2 cx)$  (Chan et al., 2007).

Once we have systematically reduced the size of our complex-valued trajectory matrix, we perform a more economical yet accurate factorization of such. The factorization involves the product of a unitary matrix  $\mathbf{Q}$ , meaning that  $\mathbf{Q}^\dagger \mathbf{Q} = \mathbf{I}$ , with  $\mathbf{I}$  being the identity matrix, and a right triangular matrix  $\mathbf{R}$

$$\mathbf{G} = \mathbf{QR} \quad (4.5)$$

Cheng and Sacchi (2016) show that performing rank-reduction on a matrix

via RQRD is about ten times faster in computation time than TSVD. Correspondingly, the computational complexity of the full and truncated SVD would require an order of  $\mathcal{O}(lx^2mx)$  and  $\mathcal{O}(k^2mx)$  operations, respectively (Golub and Van Loan, 1996). The following expression gives an estimate of the trajectory matrix as a projection onto its  $k$  rank-reduced orthonormalized basis  $\mathbf{Q}$  with dimensions  $(mx \times \kappa)$ .

$$\mathbf{H}_k = \mathbf{Q}(\mathbf{Q}^\dagger \mathbf{H}) \quad (4.6)$$

The parameter  $\kappa$  is considered to be a relaxation of the desired rank  $k$  of the data. In general, RQRD can not ensure that the approximation is of rank  $k$  since the random projection step does not constrain the rank as strongly as the SVD, given that the SVD is the optimal solution in the least-squares sense, which results in unattenuated noise evenly spread across the spectrum. Put differently, we treat  $\kappa$  as a random subset of the desired rank  $k$ , and this is crucial in achieving better reconstruction for real data. We know very little information about the rank of the field data acquired, and as a consequence, the rank  $k$  of such is rarely a priori in geophysical problems. Furthermore, there is unusually a clear cut separation of signal and noise in the singular value spectra.

The last step in the algorithm requires recovering the estimated data at a given frequency. In traditional SSA, this step entails summing along the anti-diagonals of  $\mathbf{H}_k$  from equation 3.10 and then multiplying each sum by a given weight to obtain a given entry in  $\hat{D}(x)$ . The weights are calculated in ad-

vance directly from the size of the data. Hence, this is an averaging step of each anti-diagonal proportional to its length denoted by the operator  $\mathcal{A}(\cdot)$  in equation 3.12,

$$\hat{\mathbf{D}} = \mathbf{w} \circ (\sigma_1(\mathbf{u}_1 * \mathbf{v}_1^\dagger) + \dots + \sigma_k(\mathbf{u}_k * \mathbf{v}_k^\dagger)) \quad (4.7)$$

In this formulation,  $\mathbf{w}$  are the weights and  $*$  means convolution. The overall cost of the process in equation 4.7 requires  $\mathcal{O}(nx)$  multiplications and  $\mathcal{O}(lxx)$  sums (Korobeynikov, 2009). However, the FFT efficiently computes the convolution, reducing the cost to  $\mathcal{O}(nx \log_2(k))$ .

Cheng et al. (2019) adopt the previously mentioned step to RQRD

$$\hat{\mathbf{D}} = \mathbf{w} \circ ((\mathbf{q}_1 * \mathbf{t}_1) + \dots + (\mathbf{q}_\kappa * \mathbf{t}_\kappa)) \quad (4.8)$$

$\mathbf{t}_i = \mathbf{q}_i^\dagger \mathbf{H}$  belong to the  $i$ th row of the rank-reduced orthonormalized basis  $\mathbf{Q}$  from equation 4.5. As we saw in equation 4.3, this is computed via fast matrix-vector multiplication. Thus, completely bypassing the implicit construction of any Hankel matrices in the SSA algorithm.

When handling 5D data, the 4D FFT replaces the 1D FFT in the matrix-vector products and anti-diagonal averaging steps of the rank-reduction algorithm. Level-One matrices with special structures such as Toeplitz, Hankel and circulant, are replaced by their multi-level block matrix equivalence.

### 4.2.2 Interpolation with a reinsertion algorithm

As discussed previously in Chapter 3, the less-than-ideal acquisition geometry creates sparse or incomplete matrices arising from missing observations, which in turn increases the rank of the trajectory matrix. We use the iterative algorithm described in 3.16 to recover the timing and amplitude of the missing records. All the parameters are kept constant, with the only difference being the rank-reduction operator  $\mathcal{F}(\cdot)$ . In the case of 3D data, the operator employs the SVD as a means to reduce the Hankel matrix, whereas, for 5D data, it uses the RQRD technique described by equation 4.5.

## 4.3 Results

### 4.3.1 Synthetic data

Like in Chapter 3, in this section, we evaluate the performance of the proposed 5D reconstruction algorithm on several theoretical data sets containing P-to-s receiver functions from MTZ conversions produced using the same matrix propagator approach (Dokht et al., 2016). Again, the generated synthetic events originate from a homogeneous Earth with a depth varying velocity structure (Dziewonski and Anderson, 1981), epicentral distances  $\Delta \in [45, 90]^\circ$  and a frequency band of  $\omega \in [0.1, 1.5]Hz$ . The temporal length of the window is 65s with a sampling interval of 0.1s. The generated numerical receiver functions contain three approximately linear events in the  $t - \Delta - \phi$  domain

corresponding to the 220-km, 410-km and 660-km interfaces.

The rank reduction operator  $\mathcal{F}(\cdot)$  works on  $n_\omega = 72$  frequency slices, where  $\omega \in [0.01, 0.36]Hz$  in each run for a total of  $n_{iter} = 150$  iterations by using the RQRD technique. We keep the same reinsertion weight of  $\alpha = 0.4$  to honour the original observations robustly. Lastly, we determine their theoretically optimal rank by quantifying the reconstruction quality of the output data in decibels (dB) (equation 3.17).

Equation 3.17 provides insight into the change in the accuracy of the reconstruction between 3D and 5D data sets and their corresponding algorithms while keeping the remaining terms constant. The two methods can both recover the amplitudes and timing of the discontinuities from the synthetic data. However, the simultaneous enhancement of groups of gathers outperforms single gather reconstruction.

We conclude the synthetic test by forming a theoretical seismic volume that depends on four spatial variables. This procedure creates the multi-dimensional array by embedding the 3D CRG along two additional axes for a set of eight equidistant  $x - y$  station coordinate sectors. That is, we form a group of single station gathers such that  $d(t, \Delta, \phi)$  becomes  $d(t, r_x, r_y, \Delta, \phi)$ . Consequently, the model data ( $Q_{in} = \infty$ ) is of size  $(n_t \times nr_x \times nr_y \times n\Delta \times n\phi)$ , where  $n_t = 651$ ,  $nr_x = 8$ ,  $nr_y = 8$ ,  $n\Delta = 46$  and  $n\phi = 8$ . The size of the corresponding level-four block Hankel matrices for this example is  $(1472 \times 3000)$ . Again, we would like to stress that the panels are identical before decimation due to the assumption of an azimuthally invariant 1D structure. We find that

each gather and their back-azimuth sectors are not identical after removing the observations since the decimation is random.

We assess the performance of the 5D recovery algorithm on two distinct volumes. First, we increase the rank of the seismic volumes by introducing Gaussian noise and replacing receiver functions with zero traces at random using the sampling operator  $\mathbf{S}(\cdot)$  to imitate field data acquisition surveys. In this example, the input data is 30% full and has an SNR of 0.5, which result in an input quality of  $Q_{in} = -1.14dB$  in Fig. 4.1a. Likewise, the second volume is 50% full and has an SNR of 2.0, matching to an input quality of  $Q_{in} = 1.24dB$  shown Fig. 4.1c. Figs 4.1b and c show the retrieved data for  $(nr_x = 4, nr_y = 4)$  with an output quality of  $Q_{out} = 7.04dB$  and  $Q_{out} = 9.13dB$ , respectively. These examples confirm that 5D MSSA outperforms 3D MSSA due to its ability to exploit the redundancy in the data across space.

Furthermore, for the case of  $nr_x = nr_y = n\phi = 4$ , the theoretical arrivals are sufficiently resolved with 11 singular values for the first data volume, while eight singular values are needed for the second data volume. Similar to the 3D case, a rank that exceeds the optimal systematically reduces the accuracy of the recovery by re-introducing noise.

### 4.3.2 Field data

In this section, we examine 5D FMSSA on observations from the USArray and perform the time-to-depth conversion of the enhanced records to observe the discontinuity structure bellow the array of receivers in the Yellowstone

area. For consistency, we keep only the events with ray parameters between  $0.08s/rad$  and  $0.04s/rad$ , which are ideal in the RFM (Gurrola et al., 1994).

We follow equations 2.1 to 2.4 and use equation 2.5 to assemble the 5D volumes containing information from four spatial variables while ensuring uniform sampling. This stacking process equalizes the importance for all pseudo-CRGs. Again, we then adopt the inverse distance weighting (IDW) stacking approach in Chapter 3 with a distance-dependent smoothing weight of  $P = 1$ . The sampling operator  $\mathbf{S}(\cdot)$  is a 5D array containing ones or zeros depending on whether there is an observation or not and it quantifies the degree of sparseness in the data after binning. We limit the frequency band of the input data by applying a band-pass filter with the same design as in the previous chapter. We chose  $alpha = 0.4$ ,  $n_{iter} = 150$ ,  $\omega \in [0.01, 0.36]Hz$ ,  $n_\omega = 72$  and a value of  $k = 10$  for consistency.

At last, we test the rapid, and memory-efficient recovery algorithm on a real 5D multi-linear array of receiver functions  $d(t, r_x, r_y, \Delta, \phi)$  by performing the rank-reduction step via the randomized QR decomposition (RQRD). We process data from the USArray in the western US covering the Yellowstone region. The scheme forms the tensor by embedding 3D gathers on the additional two spatial variables from 394 stations containing a total of 15100 receiver functions, before binning. Fig. 4.3a shows their original position before forming the regular grid of receivers. The binning geometry is as follows:

- Summary station longitude coordinates:

$$r_{x_{i_1}} = r_{x_0}^{min} + (i_1 - 1)\delta r_x, \quad r_{x_0}^{min} = -115.5^\circ, \quad \delta r_x = 1^\circ, \quad \text{and } i_1 =$$

$$1, \dots, nr_x = 10$$

- Summary station longitude coordinates:

$$. r_{y_{i_2}} = r_{y_0}^{min} + (i_2 - 1)\delta r_y, r_{y_0}^{min} = 40.5^\circ, \delta r_y = 1^\circ, \text{ and } i_2 = 1, \dots, nr_y =$$

$$8$$

- Epicentral distance sectors for each summary station:

$$. \Delta_{i_3} \in [\Delta_0^{min} - (2 - i_3)\delta\Delta, \Delta_0^{min} + (i_3)\delta\Delta], \Delta_0^{min} = 31^\circ, \delta\Delta = 1^\circ \text{ and}$$

$$i_3 = 1, \dots, n\Delta = 59$$

- Back-azimuth sectors for each summary station:

$$. \phi_{i_4} \in [\phi_0^{min} - (2 - i_4)\delta\phi, \phi_0^{min} + (i_4)\delta\phi], \phi_0^{min} = 45^\circ, \delta\phi = 45^\circ \text{ and}$$

$$i_4 = 1, \dots, n\phi = 8$$

After binning, we construct a 4D source-receiver grid with spatial dimensions  $(nr_x \times nr_y \times n\Delta \times n\phi)$  where  $nr_x = 10$ ,  $nr_y = 8$ ,  $n\Delta = 59$  and  $n\phi = 8$ . The associated level-four block Hankel matrices would have dimensions  $(2400 \times 4500)$ , these matrices are 600 times bigger than the level-two Hankel matrices in the 3D real data case; this is equivalent to a 59900% increase in size. Performing an SVD on such matrices would be much more expensive, hence the demand for computationally efficient algorithms. The tensor contains information from 80 summary stations, which contain a total of 28746 receiver functions. Approximately 24% of the seismic volume does not contain any information. Fig. 4.4a shows the locations of the regularly spaced summary stations and Fig. 4.4b

shows the fold in the  $r_x - r_y$  plane, the maximum fold is 404 traces, while the minimum is 258 traces.

Again, the MSSA filter parameter is  $k = 10$  for the previously stated reasons. Figs 4.5a, d and g show the results of the iterative rank-reduction method via RQRD. These gathers belong to the slices  $r_x = 5$ ,  $r_y = 4, 5, 6$  and are the same summary stations in Figs 3.3a, d and g. This is done to obtain a fair comparison of the methods. The output stacks show the suspected phases with the correct polarity and timing across all panels. We shed light on the increase in performance of the reconstruction when more spatial variables are available by directly comparing the output slices  $\phi = 45^\circ$  seen in Figs 3.4b, d and e, and in Figs 4.5a, d and g. Although the output from the 3D algorithm fills the gaps, the phases are more evident on its 5D counterpart. Figs 4.5c, f and i show the associated summary trace stacked along both spatial dimensions. In addition to the successful prediction of the timing and amplitudes of the interpolated receiver functions, the proposed method preserves the P410s and P660s phases. Again, we note the existence of a robust negative polarity double phase preceding the P660s discontinuity.

Lastly, we would like to be transparent about a challenge that comes with this method; it is very easy to mask small scale features at the cost of recovering the overall structure. We can see a decrease in amplitude from conversions from the 520-km discontinuity in Figs 4.5c, f and i; this is due to the smoothing effect created by the stacking parameter  $P$  and the bin size  $r$  in comparison to the node spacing parameters  $\delta r_x$  and  $\delta r_y$ . One could overcome these feats by choosing a value for  $P$  that exceeds the number of spatial dimensions giving

higher precedence to nearby observations and by choosing a smaller search radius to reduce the amount of overlap between adjacent nodes. Although it is possible to fine-tune these parameters to preserve and enhance local features.

## 4.4 Conclusion

The reconstruction of earthquake records via MSSA traditionally requires an SVD, which is particularly expensive for large matrices. This chapter requires the rank-reduction of a trajectory matrix that contains information from four spatial dimensions. Depending on the number of samples for each dimension, traditional MSSA could be unmanageable by standard TSVD. Here, we presented a more feasible alternative that yields satisfactory results, namely the RQRD. The results show that the method presented in this chapter can recover the amplitude and timing, which a full set of measurements would contain.

The accuracy of the algorithm is less stringent on the choice of the rank of the trajectory matrix than the TSVD conventional approach. In doing this, we achieve significant accuracy since we do not recover high levels of noise even for a higher choice of  $k$ . Additionally, it requires less memory as the level-four Hankel matrix does not need to be explicitly built. Overall, this algorithm successfully accelerated MSSA.

Synthetic and field data examples imply that the proper application of the suggested methods is arguably a viable approach for the analyses and interpretation of secondary phases from the Earth's interior, such as P-to-s converted

phases. We identify robust conversions for the 410-km and 660-km interfaces beneath Yellowstone. As expected, the reconstruction produces an extensive smoothing of the RF impulse response, masking local variations of the MTZ. For instance, the 520-km discontinuity observed in the reconstruction of 3D records is averaged laterally when applying the 5D FMSSA. Additionally, we once again distinguish a robust P660s precursor with double phase and negative polarity.

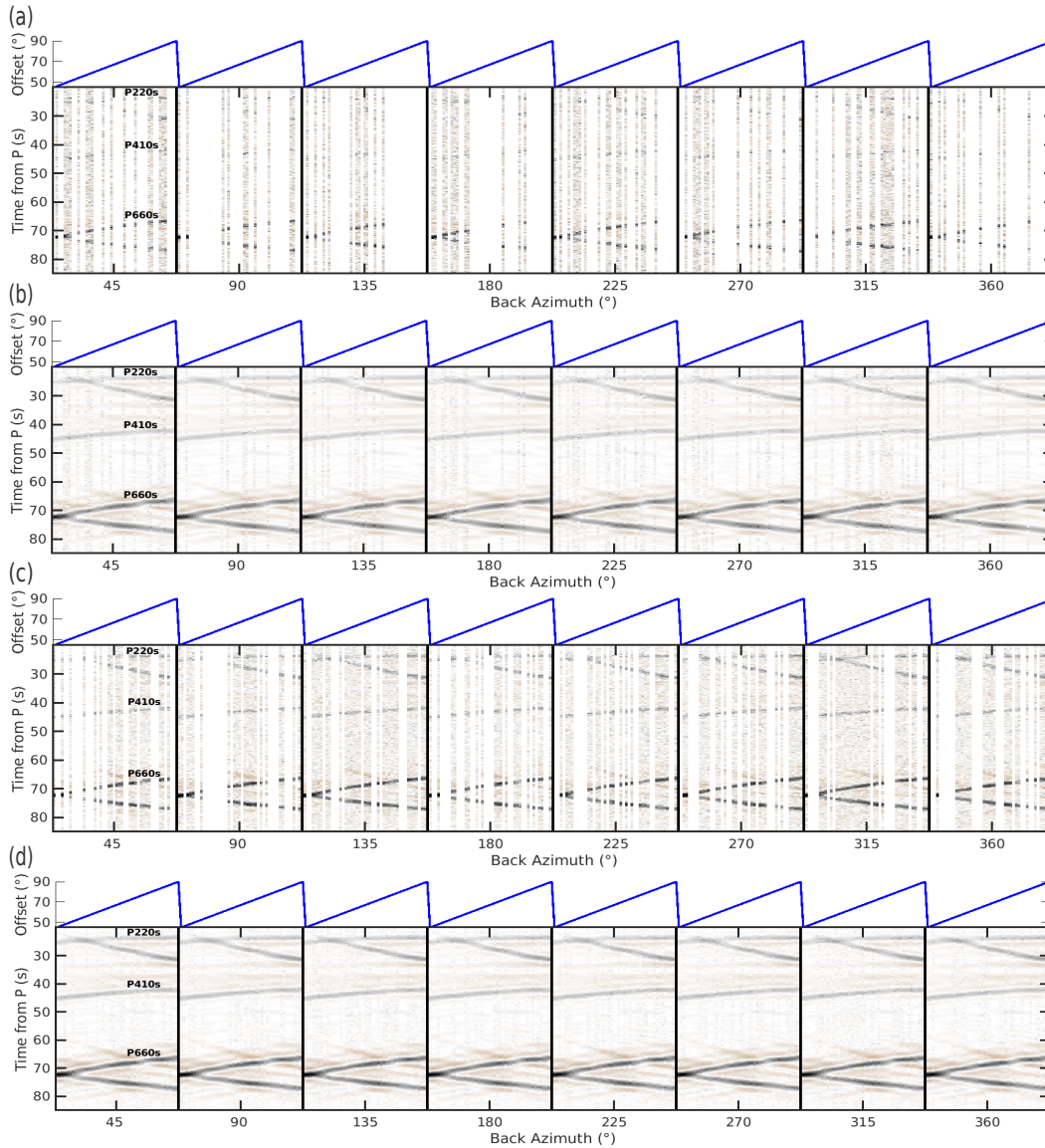


Figure 4.1: Reconstruction examples of 5D synthetic volumes from a 1D velocity structure. Single gathers from the receivers with indices  $(r_x = 4, r_y = 4)$ . (a,c) Corrupted data with 70% and 50% decimation, and an SNR of 0.5 and 2.0, respectively. (b,d) The corresponding output data after 5D MSSA using  $k = 10$ .

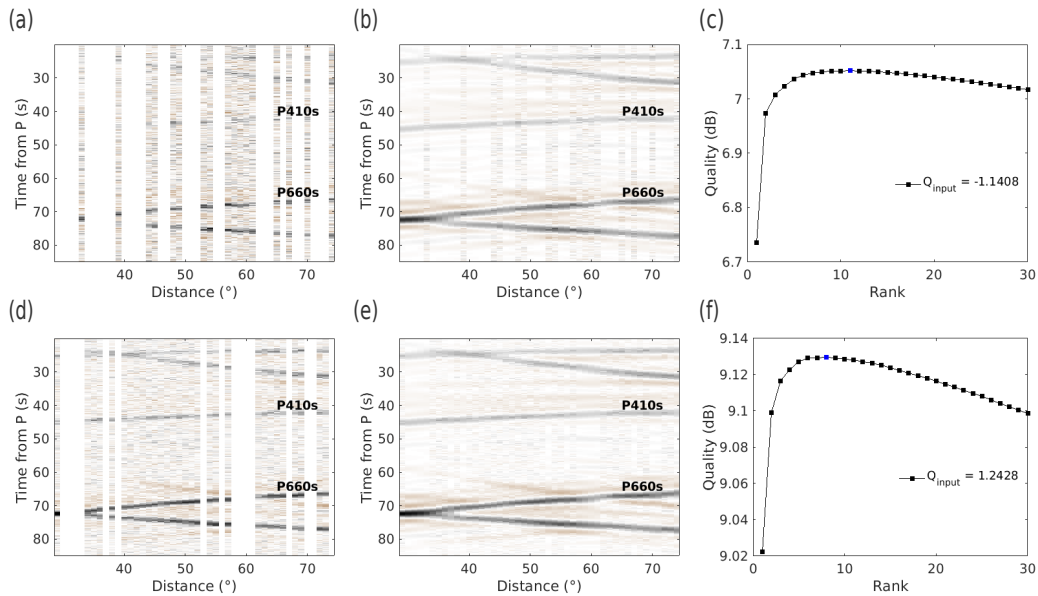


Figure 4.2: Back-azimuth slice at  $\phi = 180^\circ$  for the single station gathers shown in Fig. 4.1, and the quality of reconstruction as a function of the rank of the Hankel matrix. (a,d) Figs 4.1b and d. (b,e) Figs 4.1c and e. (c,f) Choosing  $k=8$  and  $k=10$  produces the recovery quality for the synthetics in Figs 4.1b and d, respectively. An increase in spatial redundancy translates to an increase in dB for the recovered data sets for a fixed rank. That is, the volume depending on four spatial coordinates will be more robustly enhanced than the volume depending on three spatial variables, everything else constant.

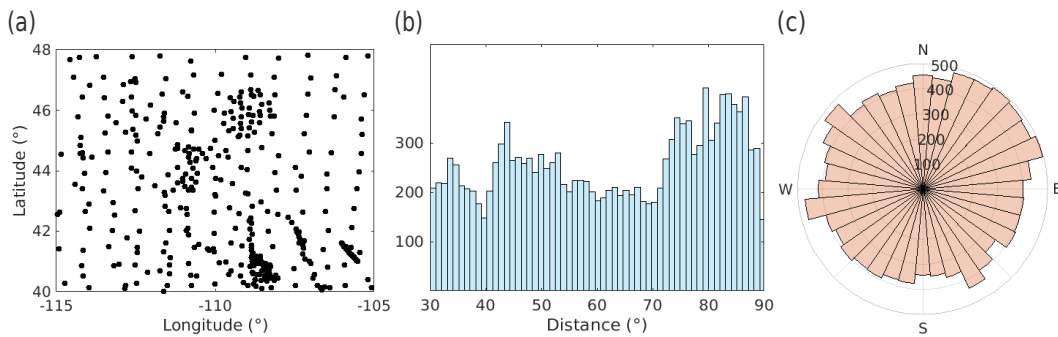


Figure 4.3: Field acquisition geometry and statistics for 5D MSSA examples. (a) Irregular distribution of stations before binning in the Latitude-Longitude plane. (b) The overall distribution of the teleseismic events' distances. The vertical axis represents the count. (c) The overall distribution of the events' back-azimuths illustrated using a linear scale.

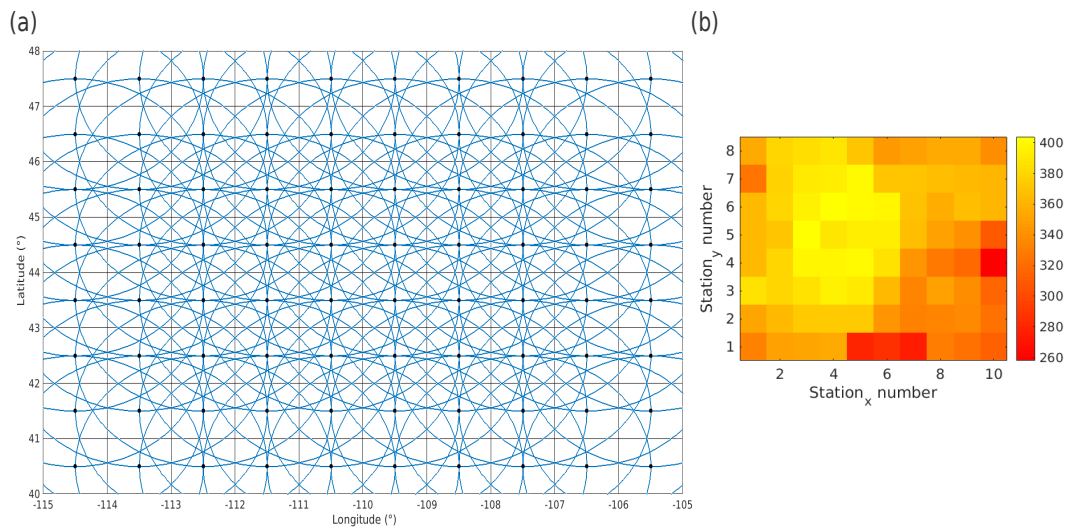


Figure 4.4: Regularly sampled data and fold, for the 5D examples. (a) Distribution of reconstructed summary stations in the regular grid. The black dots show their x-y coordinates and the blue circles correspond to a search radius of  $r = 2^\circ$ . (b) The fold map of the 5D data structure showing the station density for a given cell.

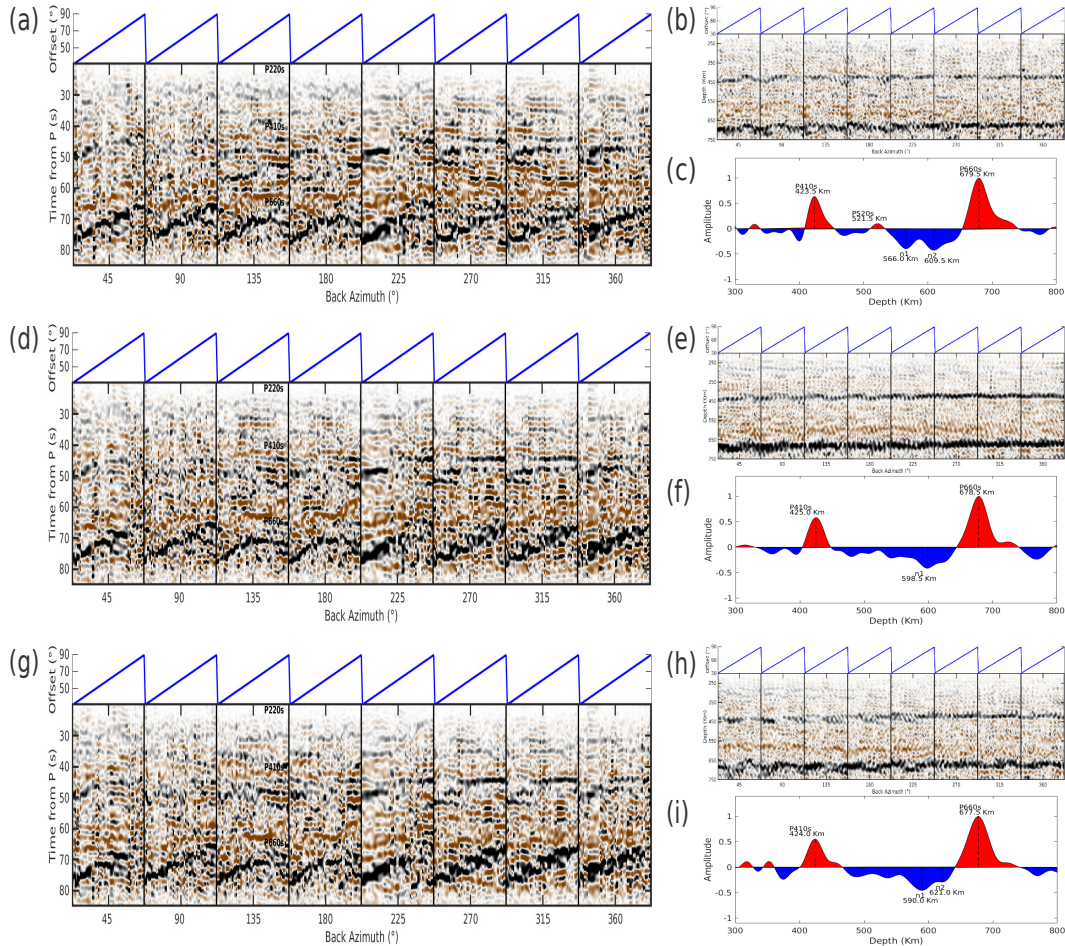


Figure 4.5: Results of 5D real data set enhancement. The field data set is shown in 4.4. (a,d,g) The retrieved data illustrated by the latitude and longitude sector pairs  $(r_x = 5, r_y = 4)$ ,  $(r_x = 5, r_y = 5)$  and  $(r_x = 5, r_y = 6)$ , respectively. The RQRD implements the rank reduction step in the algorithm 4.6. (b,e,h) Time converted output volumes. (c,f,i) Stack of the enhanced depth-converted receiver functions with discontinuity depths (black dashed lines) and Pds arrivals.

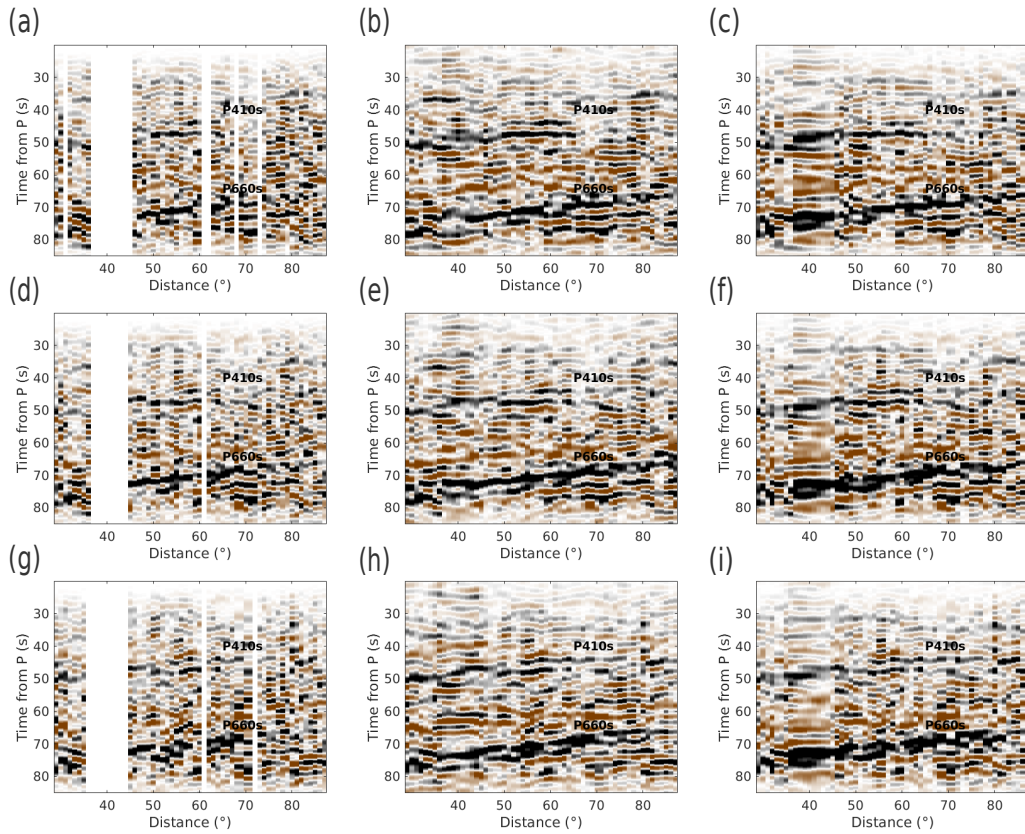


Figure 4.6: Comparison of 3D and 5D reconstruction of seismic field data for the back-azimuth bin 6 ( $315^\circ - 45^\circ$ ) of the gathers in Fig. 3.4 and Fig. 4.5 using  $\alpha = 0.4$  and  $k = 10$ . (a,d,g) Input data. Slice for  $\phi = 360^\circ$ . (b,e,h) The output data. Slice for  $\phi = 360^\circ$ , the truncated SVD performs the rank reduction step. (c,f,i) The output data via fast 5D MSSA. Slice for  $\phi = 360^\circ$ . The P410s and P660s waveforms are robustly enhanced, and a strong negative polarity P660s precursor waveform is observable across all panels at  $60s - 70s$ .

---

---

## CHAPTER 5

---

### Conclusion

#### 5.1 Summary

Throughout this thesis, we investigated MSSA as a recovery algorithm using P-to-S converted waves arising from MTZ discontinuities. MSSA is predicated on the idea under ideal conditions, the data is compressible and of low-rank. We increased the amount of data processed by increasing the dimensionality of the seismic volumes and adapted the rank-reduction techniques to recover the mantle reflectivity structure robustly. Careful mathematical treatment for building the trajectory matrix and finding a lower rank approximation of such is crucial to enhance and precondition large data sets for improving seismic imaging and our understanding of mantle structures, which in turn can tell us something about its dynamics and composition.

In Chapter 1, we give a brief overview of the mantle and its seismically discontinuous region, the MTZ. We describe the importance of performing imaging

studies of the interior of the Earth and outline some of the phases previously observed on a global average. Next, we introduce the RFM as a tool in global seismology to examine the seismic structure of the Earth at mantle depths with some examples in the literature. Receiver function studies are typically compromised by the underlying geometry of the secondary conversions. Receivers or stations need to be placed approximately above the area of interest, and we have no control over any source parameters such as occurrence, location or magnitude. Although there is a substantial increase in the amount of data collected and networks of arrays deployed around the world, the acquisition geometry is still affected by terrain, logistic and economic complications, additional to the high levels of noise intrinsic to receiver functions.

With the recent availability of dense seismological networks of arrays, researchers in the field of global seismology have developed many methods to reconstruct seismic data. Reconstruction of wavefields sensed by grids of arrays will improve our understanding of the Earth's structure beneath the array. In Chapter 2, we introduced a practical and intuitive way to construct multi-dimensional gathers containing receiver functions. The presented binning method performs an IDW-based station-event stacking of a particular location of interest, to increase the SNR and robustness of the conversions in the existing observations. For all nearby stations inside a search radius, our technique sorts the receiver functions by their distance and back-azimuth. It equalizes station importance by normalizing the number of events per pseudo-CRG. Various parameters such as bin size, degree of smoothing, overlap and spacing control the ensemble of the multi-linear arrays and have a direct im-

impact on the quality of reconstruction and the scale of the recovered seismic features. These assembly parameters can be tailored to mimic particular networks of arrays, such as the USArray, since the receiver function volumes base their design on the spatial sampling regularity required by singular spectrum analysis. This chapter shows we can build 3D and 5D receiver function volumes and simultaneously reconstruct the wavefields recorded by all the receivers in the grid. These volumes provide insights on structural variations with back-azimuth and offset for different receivers and permit the imaging of the reflectivity underneath the stations.

The interpolation and random noise attenuation of uniformly spaced data is an essential topic in seismic data processing. Numerous studies have addressed this problem in the field of exploration seismology, but there are not many reports of algorithms proposed for earthquake data. In chapter 3, we studied the use of MSSA as a proof of concept to reconstruct 3D CRGs of receiver functions sorted by epicentral distance and back-azimuth. MSSA is a technique that yields an estimate of a low-rank version of the observed signals, and it relies on the spatial predictability of our model. The truncated SVD performs the rank reduction step in the frequency-space domain in this chapter. The rank of the theoretical level-2 Hankel matrix is related to the number of expected linear events produced by MTZ interfaces. The recovery algorithm operates on synthetic record sections and observations from the Yellowstone area. We test the method on a numerically generated data set using a 1D global model of the Earth. In these examples, we corrupt the generated data with random noise and decimation. We also construct pseudo-CRGs from P-

to-S converted waves recorded by the USArray using the procedure described in Chapter 2. We apply MSSA to remove random noise, reconstruct gaps in the data, and enhance the robustness of the secondary phases. In both cases, comparisons with raw data, MSSA reconstructed data shows discernible MTZ secondary phases attributable to incoherent noise filtering and correct timing and amplitude recovery of the receiver functions.

In Chapter 4, we include the x-y coordinates of the stations to construct and enhance 5D seismic volumes. 5D MSSA requires a different mathematical approach due to the computational complexity of using the truncated SVD as the rank reduction approximation. A randomized QR decomposition performs the low-rank approximation step and avoids building and thus storing the huge level-4 Hankel matrix using a fast vector-matrix multiplication technique. The results from including their coordinates in the recovery algorithm are significantly better than 3D reconstruction. The improvement in the reconstruction quality is a consequence of the addition of more information per frequency slice in the analysis. We tested FMSSA using numerically generated synthetic data and field data from the USArray. Our analysis shows that it is possible to simultaneously suppress white Gaussian noise while filling gaps in the records. The results show that using RQRD is more computationally efficient than using truncated SVD without compromising signal recovery. The proposed algorithm has a few parameters to vary. Such are the pseudo-CRG gather spacing, search radiuses and the IDW smoothing parameter. These parameters dictate the ability to capture small scale features or the overall seismic structure beneath the grid of receivers. Synthetic and real data ex-

amples suggest that the precise application of FMSSA is a correct approach for preconditioning waveforms from secondary conversions. In this study, we focus on the radial component, keeping in mind that the reconstruction algorithm can equally enhance the other components. The improvement in the receiver functions makes FMSSA an appealing tool to use in seismic imaging using receiver functions.

## 5.2 Contributions and limitations

The contributions of this thesis are as follows. Firstly, we present a method to assemble regularly spaced multi-linear arrays of Receiver functions. The suggested 3D and 5D binning procedures equalize the station importance and the effects from varying distances and back-azimuths by incorporating IDW stacking. Secondly, we prove that MSSA can reconstruct approximately linear events arising from MTZ secondary conversions. 2D MSSA works in the  $f - xy$  domain and implements the truncated SVD as the rank reduction step. Lastly, this research extended MSSA, and it is capable of handling receiver functions that depend on one 4 spatial coordinates. This generalization required a mathematical treatment in which reduces the computational complexity by implementing the RQRD as the rank-reduction step. The recovery algorithms examine numerically generated and field data. Both methodologies accurately recover the timing and amplitude of the missing observations while enhancing P-to-s converted phases contained in the seismic records. These observations consistently suggest a P660s precursor with double phase and negative polarity

underneath Yellowstone. Ancient oceanic material, a subducting slab, plume remnants, partial melt, and an increase in water content may be associated with the signals from these MTZ zone interfaces. This study only recovered the radial component as a proof of concept, knowing that it can resolve the remaining components in the same manner without any complications.

The reconstruction of multidimensional earthquake records relies on many factors that dictate the quality of the output data. Fundamental limitations are the amount of available unprocessed receiver functions as a consequence of acquisition geometry constraints. Mapping the seismic structure of the Earth strongly depends on the placement of arrays of receivers. As we saw, individual raw stations need to be combined with nearby stations to form a pseudo-CRG. Otherwise, the seismic volumes are too sparse, making MSSA not feasible. Additional challenges that come with secondary seismic phases are the low SNR and interfering seismic arrivals. The constructions of the multi-linear gathers need a careful selection of the binning parameters to mimic the acquisition parameter of the underlying network of arrays of receivers. However, the parameter selection comes with a trade-off between the scale of the recovered seismic features and the number of missing observations. An acquisition design with receivers too closely spaced could resolve small local features, but it may simply not be possible to reconstruct due to the amount of decimation. The desired rank is not a priori for field data, so some experimentation is needed. Many reports show that  $k$  should be about 2-3 times larger than the number of actual phases due to real data not being entirely explained by simple linear events and lateral variations of amplitude. More fundamentally,

only structurally simple data can be enhanced, and the output tends to be smooth.

### 5.3 Future work

The method presented in this thesis will benefit future analyses of seismic phases originating at depths below the crust, particularly for studies where sources and receivers are irregularly spaced. Future investigations in the reconstruction of secondary conversions may head towards more sophisticated migration methods than the ones presented in this work. For instance, they could incorporate 3D regional seismic models to place the receiver function in the correct location where the P-to-s conversion occurs. This type of imaging provides a better estimate of the reflectivity structure underneath the grid of receivers. In the same manner, the enhanced receiver functions can be used to estimate for a regional shear-wave seismic velocity model.

Some other aspects, such as the distribution of earthquakes and stations, can be studied in more detail to select the optimal binning parameters that can best resolve features without compromising the quality of reconstruction. In this investigation, we sacrificed preserving small scale features when using 5D reconstruction for a more consistent smooth model. Future studies can window the data to improve the reconstruction algorithms by approximating nonlinear events in the window of analysis. The works presented here assume the signals are composed of purely linear events immersed in random noise. Future investigations can generalize the model to include both random and

erratic noise with unknown distributions as it is the case with field data.

Studies focusing on the interpretation of seismic structures of the MTZ can implement the suggested recovery techniques to several networks of arrays around the globe. Furthermore, future work can explore resolving the other two horizontal components of receiver functions. Lastly, we suggest the application of MSSA to other seismological observations such as SS and PP precursors, triplications and ScS reverberations.

# Bibliography

- Abma, R., and J. Claerbout, 1995, Lateral prediction for noise attenuation by t-x and f-x techniques: *Geophysics*, **60**, 1887–1896.
- Abma, R., and N. Kabir, 2006, 3d interpolation of irregular data with a POCS algorithm: *Geophysics*, **71**, E91–E97.
- Acar, E., and B. Yener, 2009, Unsupervised multiway data analysis: A literature survey: *IEEE Transactions on Knowledge and Data Engineering*, **21**, no. 1, 6–20.
- Aharchaou, M., and A. Levander, 2016, A compressive sensing approach to the high-resolution linear Radon transform: application on teleseismic wavefields: *Geophysical Journal International*, **207**, 811–822.
- Ammon, C., 1991, The isolation of receiver effects from teleseismic p waveforms: *Bulletin of the Seismological Society of America*, **81**, 2504–2510.
- Ammon, C. J., G. E. Randall, and G. Zandt, 1990, On the nonuniqueness of receiver function inversions: *Journal of Geophysical Research: Solid Earth*, **95**, 15303–15318.
- An, Y., Y. J. Gu, and M. D. Sacchi, 2007, Imaging mantle discontinuities using least squares Radon transform: *Journal of Geophysical Research: Solid*

- Earth, **112**.
- Andrews, H. C., and C. L. Patterson, 1975, Outer product expansions and their uses in digital image processing: *The American Mathematical Monthly*, **82**, 1–13.
- Birch, F., 1961, Composition of the Earth's Mantle: *Geophysical Journal International*, **4**, 295–311.
- Bostock, M., 1998, Mantle stratigraphy and evolution of the slave province: *Journal of Geophysical Research: Solid Earth*, **103**, 21183–21200.
- Broomhead, D. S., and G. P. King, 1986, Extracting qualitative dynamics from experimental data: *Physica D: Nonlinear Phenomena*, **20**, 217–236.
- Buttkus, B., 1986, Ten years of the Gräfenberg array: defining the frontiers of broadband seismology: *Bundesanstalt für Geowissenschaften und Rohstoffe*.
- Cadzow, J. A., 1988, Signal enhancement—a composite property mapping algorithm: *IEEE Transactions on Acoustics, Speech, and Signal Processing*, **36**, 49–62.
- Canales, L. L., 1984, Random noise reduction, *in* SEG Technical Program Expanded Abstracts 1984: Society of Exploration Geophysicists, 525–527.
- Candès, E. J., L. Demanet, D. Donoho, and L. Ying, 2005, Fast discrete curvelet transforms: tech. report, Calif. Inst. of Tech., [www.curvelet.org](http://www.curvelet.org).
- Carozzi, F., and M. D. Sacchi, 2019, Robust tensor-completion algorithm for 5d seismic-data reconstruction: *Geophysics*, **84**, V97–V109.
- Cassidy, J. F., 1992, Numerical experiments in broadband receiver function analysis: *Bulletin of the Seismological Society of America*, **82**, 1453–1474.
- Chai, C., C. J. Ammon, M. Maceira, and R. B. Herrmann, 2015, Inverting

- interpolated receiver functions with surface wave dispersion and gravity: Application to the western us and adjacent canada and mexico: *Geophysical Research Letters*, **42**, 4359–4366.
- Chan, R., Hon-Fu, and X.-Q. Jin, 2007, An introduction to iterative Toeplitz solvers: *SIAM*, **5**.
- Chen, Y., M. Bai, and Y. Chen, 2019, Obtaining free USArray data by multi-dimensional seismic reconstruction: *Nature communications*, **10**, 1–13.
- Cheng, J., M. Sacchi, and J. Gao, 2019, Computational efficient multidimensional singular spectrum analysis for prestack seismic data reconstruction: *Geophysics*, **84**, V111–V119.
- Cheng, J., and M. D. Sacchi, 2016, Fast dual-domain reduced-rank algorithm for 3d deblending via randomized qr decomposition: *Geophysics*, **81**, V89–V101.
- Chiron, L., M. A. van Agthoven, B. Kieffer, C. Rolando, and M.-A. Delsuc, 2014, Efficient denoising algorithms for large experimental datasets and their applications in Fourier transform ion cyclotron resonance mass spectrometry: *Proceedings of the National Academy of Sciences*, **111**, 1385–1390.
- Darche, G., 1990, Spatial interpolation using a fast parabolic transform, *in* SEG Technical Program Expanded Abstracts 1990: Society of Exploration Geophysicists, 1647–1650.
- Deuss, A., 2009, Global observations of mantle discontinuities using ss and pp precursors: *Surveys in geophysics*, **30**, 301–326.
- Deuss, A., and J. Woodhouse, 2001, Seismic observations of splitting of the mid-transition zone discontinuity in earth’s mantle: *Science*, **294**, 354–357.

- Dokht, R. M., Y. J. Gu, and M. D. Sacchi, 2016, Singular spectrum analysis and its applications in mapping mantle seismic structure: *Geophysical Journal International*, **208**, 1430–1442.
- Downton, J., B. Durrani, L. Hunt, S. Hadley, and M. Hadley, 2008, 5d interpolation, pstm and avo inversion, *in* SEG Technical Program Expanded Abstracts 2008: SEG, 237–241.
- Dueker, K. G., and A. F. Sheehan, 1997, Mantle discontinuity structure from midpoint stacks of converted p to s waves across the yellowstone hotspot track: *Journal of Geophysical Research: Solid Earth*, **102**, 8313–8327.
- Dziewonski, A. M., and D. L. Anderson, 1981, Preliminary reference earth model: *Physics of the earth and planetary interiors*, **25**, 297–356.
- Eckart, C., and G. Young, 1936, The approximation of one matrix by another of lower rank: *Psychometrika*, **1**, 211–218.
- Farra, V., and L. Vinnik, 2000, Upper mantle stratification by P and S receiver functions: *Geophysical Journal International*, **141**, 699–712.
- Frassetto, A., G. Zandt, H. Gilbert, T. Owens, and C. Jones, 2010, Improved imaging with phase-weighted common conversion point stacks of receiver functions: *Geophysical Journal International*, **182**, 368–374.
- Freire, S. L., and T. J. Ulrych, 1988, Application of singular value decomposition to vertical seismic profiling: *Geophysics*, **53**, 778–785.
- Gao, J., M. D. Sacchi, and X. Chen, 2013a, A fast reduced-rank interpolation method for prestack seismic volumes that depend on four spatial dimensions: *Geophysics*, **78**, V21–V30.
- Gao, J., A. Stanton, M. Naghizadeh, M. D. Sacchi, and X. Chen, 2013b,

- Convergence improvement and noise attenuation considerations for beyond alias projection onto convex sets reconstruction: *Geophysical prospecting*, **61**, 138–151.
- Ghaderpour, E., W. Liao, and M. P. Lamoureux, 2018, Antileakage least-squares spectral analysis for seismic data regularization and random noise attenuation: *Geophysics*, **83**, V157–V170.
- Golub, G. H., and C. F. Van Loan, 1996, *Matrix computations*, Johns Hopkins University Press, Baltimore, MD.
- Gu, Y., A. M. Dziewonski, and C. B. Agee, 1998, Global de-correlation of the topography of transition zone discontinuities: *Earth and Planetary Science Letters*, **157**, 57–67.
- Gu, Y. J., and M. Sacchi, 2009, Radon transform methods and their applications in mapping mantle reflectivity structure: *Surveys in Geophysics*, **30**, 327–354.
- Gu, Y. J., Y. Zhang, M. D. Sacchi, Y. Chen, and S. Contenti, 2015, Sharp mantle transition from cratons to Cordillera in southwestern Canada: *Journal of Geophysical Research: Solid Earth*, **120**, 5051–5069.
- Gurrola, H., G. E. Baker, and J. B. Minster, 1995, Simultaneous time-domain deconvolution with application to the computation of receiver functions: *Geophysical Journal International*, **120**, 537–543.
- Gurrola, H., J. Minster, and T. Owens, 1994, The use of velocity spectrum for stacking receiver functions and imaging upper mantle discontinuities: *Geophysical Journal International*, **117**, 427–440.
- Halko, N., P.-G. Martinsson, and J. A. Tropp, 2011, Finding structure with

- randomness: Probabilistic algorithms for constructing approximate matrix decompositions: SIAM review, **53**, 217–288.
- Hansen, P. C., 1987, The truncated svd as a method for regularization: Math-SciNet zbMATH, **27**, 534–553.
- Hassani, H., A. Dionisio, and M. Ghodsi, 2010, The effect of noise reduction in measuring the linear and nonlinear dependency of financial markets: Nonlinear Analysis: Real World Applications, **11**, 492–502.
- Hassani, H., et al., 2007, Singular spectrum analysis: Methodology and comparison: Technical report, University Library of Munich, Germany.
- Hassani, H., S. Heravi, and A. Zhigljavsky, 2013, Forecasting uk industrial production with multivariate singular spectrum analysis: Journal of Forecasting, **32**, 395–408.
- Hassani, H., and D. Thomakos, 2010, A review on singular spectrum analysis for economic and financial time series: Statistics and its Interface, **3**, 377–397.
- Helfrich, G., and C. R. Bina, 1994, Frequency dependence of the visibility and depths of mantle seismic discontinuities: Geophysical research letters, **21**, 2613–2616.
- Hennenfent, G., and F. J. Herrmann, 2008, Simply denoise: Wavefield reconstruction via jittered undersampling: Geophysics, **73**, V19–V28.
- Herlocker, J. L., J. A. Konstan, L. G. Terveen, and J. T. Riedl, 2004, Evaluating collaborative filtering recommender systems: ACM Trans. Inf. Syst., **22**, 5–53.
- Herrmann, F. J., and G. Hennenfent, 2008, Non-parametric seismic data recov-

- ery with curvelet frames: *Geophysical Journal International*, **173**, 233–248.
- Herrmann, F. J., D. Wang, G. Hennenfent, and P. P. Moghaddam, 2008, Curvelet-based seismic data processing: A multiscale and nonlinear approach: *Geophysics*, **73**, A1–A5.
- Hu, S., X. Jiang, L. Zhu, and H. Yao, 2018, Wavefield reconstruction of teleseismic receiver function with the stretching-and-squeezing interpolation method: *Seismological Research Letters*, **90**, 716–726.
- Hunt, L., J. Downton, S. Reynolds, S. Hadley, D. Trad, and M. Hadley, 2010, The effect of interpolation on imaging and AVO: A Viking case study: *Geophysics*, **75**, WB265–WB274.
- Ita, J., and L. Stixrude, 1992, Petrology, elasticity, and composition of the mantle transition zone: *Journal of Geophysical Research: Solid Earth*, **97**, 6849–6866.
- Ito, E., and T. Katsura, 1989, A temperature profile of the mantle transition zone: *Geophysical Research Letters*, **16**, 425–428.
- Jiang, T., B. Gong, F. Qiao, Y. Jiang, A. Chen, D. Hren, and Z. Meng, 2017, Compressive seismic reconstruction with extended pocs for arbitrary irregular acquisition, *in* SEG Technical Program Expanded Abstracts 2017: SEG, 4272–4277.
- Kennett, B. L. N., E. R. Engdahl, and R. Buland, 1995, Constraints on seismic velocities in the Earth from traveltimes: *Geophysical Journal International*, **122**, 108–124.
- Kondrashov, D., Y. Shprits, and M. Ghil, 2010, Gap filling of solar wind data by singular spectrum analysis: *Geophysical research letters*, **37**.

- Korobeynikov, A., 2009, Computation-and space-efficient implementation of ssa: arXiv preprint arXiv:0911.4498.
- Kreimer, N., and M. D. Sacchi, 2012, A tensor higher-order singular value decomposition for prestack seismic data noise reduction and interpolation: *Geophysics*, **77**, V113–V122.
- Kreimer, N., A. Stanton, and M. D. Sacchi, 2013, Tensor completion based on nuclear norm minimization for 5d seismic data reconstruction: *Geophysics*, **78**, V273–V284.
- Lahmiri, S., 2018, Minute-ahead stock price forecasting based on singular spectrum analysis and support vector regression: *Applied Mathematics and Computation*, **320**, 444–451.
- Langston, C. A., 1977, Corvallis, oregon, crustal and upper mantle receiver structure from teleseismic p and s waves: *Bulletin of the Seismological Society of America*, **67**, 713–724.
- , 1979, Structure under Mount Rainier, Washington, inferred from teleseismic body waves: *Journal of Geophysical Research: Solid Earth*, **84**, 4749–4762.
- , 1981, Evidence for the subducting lithosphere under southern vancouver island and western oregon from teleseismic p wave conversions: *Journal of Geophysical Research: Solid Earth*, **86**, 3857–3866.
- , 1989, Scattering of teleseismic body waves under pasadena, california: *Journal of Geophysical Research: Solid Earth*, **94**, 1935–1951.
- Lawrence, J. F., and P. M. Shearer, 2006, A global study of transition zone thickness using receiver functions: *Journal of Geophysical Research: Solid*

- Earth, **111**.
- Leles, M. C., A. S. Cardoso, M. G. Moreira, E. F. Sbruzzi, C. L. Nascimento, and H. N. Guimarães, 2018, A singular spectrum analysis based trend-following trading system: 2018 Annual IEEE International Systems Conference (SysCon), IEEE, 1–5.
- Li, X., and X. Yuan, 2003, Receiver functions in northeast china—implications for slab penetration into the lower mantle in northwest pacific subduction zone: *Earth and Planetary Science Letters*, **216**, 679–691.
- Liberty, E., F. Woolfe, P.-G. Martinsson, V. Rokhlin, and M. Tygert, 2007a, Randomized algorithms for the low-rank approximation of matrices: *Proceedings of the National Academy of Sciences*, **104**, 20167–20172.
- , 2007b, Randomized algorithms for the low-rank approximation of matrices: *Proceedings of the National Academy of Sciences*, **104**, 20167–20172.
- Ligorria, J. P., and C. J. Ammon, 1999, Iterative deconvolution and receiver-function estimation: *Bulletin of the seismological Society of America*, **89**, 1395–1400.
- Liu, B., and M. D. Sacchi, 2004, Minimum weighted norm interpolation of seismic records: *Geophysics*, **69**, 1560–1568.
- Liu, Y., Y. Li, P. Nie, and Q. Zeng, 2013, Spatio-temporal time-frequency peak filtering method for seismic random noise reduction: *IEEE Geoscience and Remote Sensing Letters*, **10**, 756–760.
- Meltzer, A., R. Rudnick, P. Zeitler, A. Levander, G. Humphreys, K. Karlstrom, E. Ekstrom, C. Carlson, T. Dixon, M. Gurnis, et al., 1999, The USArray initiative: *Geological Society of America TODAY*, **9**, 8–10.

- Menke, W., 1991, Applications of the pocs inversion method to interpolating topography and other geophysical fields: *Geophysical Research Letters*, **18**, 435–438.
- Miranda, F., 2005, Seismic data reconstruction of primaries and multiples, *in* SEG Technical Program Expanded Abstracts 2004: SEG, 2100–2103.
- Morita, Y., 1996, The characteristics of J-array seismograms: *Journal of Physics of the Earth*, **44**, 657–668.
- Naghizadeh, M., 2012, Seismic data interpolation and denoising in the frequency-wavenumber domain: *Geophysics*, **77**, V71–V80.
- Naghizadeh, M., and M. D. Sacchi, 2007, Multistep autoregressive reconstruction of seismic records: *Geophysics*, **72**, V111–V118.
- , 2008, f-x adaptive seismic-trace interpolation: *Geophysics*, **74**, V9–V16.
- , 2010a, Beyond alias hierarchical scale curvelet interpolation of regularly and irregularly sampled seismic data: *Geophysics*, **75**, WB189–WB202.
- , 2010b, Seismic data reconstruction using multidimensional prediction filters: *Geophysical Prospecting*, **58**, 157–173.
- Neal, S. L., and G. L. Pavlis, 1999, Imaging p-to-s conversions with multichannel receiver functions: *Geophysical research letters*, **26**, 2581–2584.
- Nekrutkin, V., 1996, Theoretical properties of the” caterpillar” method of time series analysis: *Proceedings of 8th Workshop on Statistical Signal and Array Processing*, IEEE, 395–397.
- O’Leary, D. P., and J. A. Simmons, 1981, A bidiagonalization-regularization procedure for large scale discretizations of ill-posed problems: *SIAM Journal on Scientific and Statistical Computing*, **2**, 474–489.

- Onajite, E., 2014, Chapter 6 - understanding cmp binning and sorting, *in* Seismic Data Analysis Techniques in Hydrocarbon Exploration: Elsevier, 87 – 92.
- Oropeza, V., and M. Sacchi, 2011, Simultaneous seismic data denoising and reconstruction via multichannel singular spectrum analysis: *Geophysics*, **76**, V25–V32.
- Owens, T. J., 1985, Determination of crustal and upper mantle structure from analysis of broadband teleseismic p-waveforms: PhD thesis, Department of Geology and Geophysics, The University of Utah.
- Owens, T. J., and R. S. Crosson, 1988, Shallow structure effects on broadband teleseismic p waveforms: *Bulletin of the Seismological Society of America*, **78**, 96–108.
- Owens, T. J., R. S. Crosson, and M. A. Hendrickson, 1988, Constraints on the subduction geometry beneath western Washington from broadband teleseismic waveform modeling: *Bulletin of the Seismological Society of America*, **78**, 1319–1334.
- Owens, T. J., S. R. Taylor, and G. Zandt, 1987, Crustal structure at regional seismic test network stations determined from inversion of broadband teleseismic p waveforms: *Bulletin of the Seismological Society of America*, **77**, 631–662.
- Ozbek, A., A. K. Ozdemir, and M. Vassallo, 2009, Interpolation by matching pursuit, *in* SEG Technical Program Expanded Abstracts 2009: SEG, 3254–3258.
- Ramírez, A. C., and A. B. Weglein, 2009, Green’s theorem as a comprehen-

- sive framework for data reconstruction, regularization, wavefield separation, seismic interferometry, and wavelet estimation: A tutorial: *Geophysics*, **74**, W35–W62.
- Ramírez, A. C., A. B. Weglein, and K. Hokstad, 2006, Near offset data extrapolation, *in* SEG Technical Program Expanded Abstracts 2006: Society of Exploration Geophysicists, 2554–2558.
- Read, P., 1993, Phase portrait reconstruction using multivariate singular systems analysis: *Physica D: Nonlinear Phenomena*, **69**, 353–365.
- Revenaugh, J., and T. H. Jordan, 1991, Mantle layering from scs reverberations: 3. the upper mantle: *Journal of Geophysical Research: Solid Earth*, **96**, 19781–19810.
- Ringwood, A., 1991, Phase transformations and their bearing on the constitution and dynamics of the mantle: *Geochimica et Cosmochimica Acta*, **55**, 2083 – 2110.
- Rokhlin, V., A. Szlam, and M. Tygert, 2009, A randomized algorithm for principal component analysis: *SIAM Journal on Matrix Analysis and Applications*, **31**, 1100–1124.
- Ronen, J., 1987, Wave-equation trace interpolation: *Geophysics*, **52**, 973–984.
- Sacchi, M. D., et al., 2009, Fx singular spectrum analysis: CSPG CSEG CWLS Convention, 392–395.
- Sacchi, M. D., J. Gao, A. Stanton, and J. Cheng, 2015, Tensor factorization and its application to multidimensional seismic data recovery, *in* SEG Technical Program Expanded Abstracts 2015: 4827–4831.
- Sacchi, M. D., and B. Liu, 2005, Minimum weighted norm wavefield recon-

- struction for a va imaging: *Geophysical Prospecting*, **53**, 787–801.
- Sacchi, M. D., and M. Porsani, 1999, Fast high resolution parabolic Radon transform, *in* SEG Technical Program Expanded Abstracts 1999: Society of Exploration Geophysicists, 1477–1480.
- Sacchi, M. D., and T. J. Ulrych, 1995, High-resolution velocity gathers and offset space reconstruction: *Geophysics*, **60**, 1169–1177.
- Sacchi, M. D., T. J. Ulrych, and C. J. Walker, 1998, Interpolation and extrapolation using a high-resolution discrete Fourier transform: *IEEE Transactions on Signal Processing*, **46**, 31–38.
- Sanei, S., M. Ghodsi, and H. Hassani, 2011, An adaptive singular spectrum analysis approach to murmur detection from heart sounds: *Medical engineering & physics*, **33**, 362–367.
- Schneider, S., C. Thomas, R. M. H. Dokht, Y. J. Gu, and Y. Chen, 2017, Improvement of coda phase detectability and reconstruction of global seismic data using frequency-wavenumber methods: *Geophysical Journal International*, **212**, 1288–1301.
- Schultz, R., and Y. Gu, 2013, Flexible, inversion-based Matlab implementation of the Radon transform: *Computers and Geosciences*, **52**, 437–442.
- Shearer, P. M., and T. G. Masters, 1992, Global mapping of topography on the 660-km discontinuity: *Nature*, **355**, 791.
- Sheldrake, K. P., C. Marcinkovich, and T. Tanimoto, 2002, Regional wavefield reconstruction for teleseismic p-waves and surface waves: *Geophysical research letters*, **29**, 39–1.
- Shen, X., H. Zhou, and H. Kawakatsu, 2008, Mapping the upper mantle discon-

- tinuities beneath china with teleseismic receiver functions: *Earth, planets and space*, **60**, 713–719.
- Shepard, D., 1968, A two-dimensional interpolation function for irregularly-spaced data: *Proceedings of the 1968 23rd ACM national conference*, ACM, 517–524.
- Song, P., X. Zhang, Y. Liu, and J. Teng, 2017, Moho imaging based on receiver function analysis with teleseismic wavefield reconstruction: Application to south china: *Tectonophysics*, **718**, 118–131.
- Spitz, S., 1991, Seismic trace interpolation in the fx domain: *Geophysics*, **56**, 785–794.
- Stepanov, D., and N. Golyandina, 2005, Variants of the Caterpillar-SSA method for forecast of multidimensional time series: *Proceedings of IV International Conference on System Identification and Control Problems (SICPRO 05)*, 1831–1848.
- Thomakos, D. D., T. Wang, and L. T. Wille, 2002, Modeling daily realized futures volatility with singular spectrum analysis: *Physica A: Statistical Mechanics and its Applications*, **312**, 505–519.
- Trad, D., 2009, Five-dimensional interpolation: Recovering from acquisition constraints: *Geophysics*, **74**, no. 6, V123–V132.
- Trad, D., T. Ulrych, and M. Sacchi, 2003, Latest views of the sparse Radon transform: *Geophysics*, **68**, 386–399.
- Trickett, S., 2008, F-xy cadzow noise suppression, *in* SEG Technical Program Expanded Abstracts 2008: Society of Exploration Geophysicists, 2586–2590.
- Trickett, S., L. Burroughs, A. Milton, L. Walton, and R. Dack, 2010, Rank-

- reduction-based trace interpolation, *in* SEG Technical Program Expanded Abstracts 2010: Society of Exploration Geophysicists, 3829–3833.
- Trickett, S. R., 2003, F-xy eigenimage noise suppression: *Geophysics*, **68**, 751–759.
- Vautard, R., P. Yiou, and M. Ghil, 1992, Singular-spectrum analysis: A toolkit for short, noisy chaotic signals: *Physica D: Nonlinear Phenomena*, **58**, 95–126.
- Ventosa, S., and B. Romanowicz, 2015, Extraction of weak PcP phases using the slant-stacklet transform I: method and examples: *Geophysical Journal International*, **201**, 207–223.
- Wang, J., M. Ng, and M. Perz, 2010, Seismic data interpolation by greedy local Radon transform: *Geophysics*, **75**, WB225–WB234.
- Whiteside, W., M. Guo, J. Sun, and B. Wang, 2014, 5d data regularization using enhanced antileakage Fourier transform: SEG Technical Program Expanded Abstracts 2014, 3616–3620.
- Wilson, C., and A. Guitton, 2007, Teleseismic wavefield interpolation and signal extraction using high-resolution linear Radon transforms: *Geophysical Journal International*, **168**, 171–181.
- Xu, S., Y. Zhang, and G. Lambaré, 2010, Antileakage Fourier transform for seismic data regularization in higher dimensions: *Geophysics*, **75**, WB113–WB120.
- Xu, S., Y. Zhang, D. Pham, and G. Lambare, 2005, Antileakage Fourier transform for seismic data regularization: *Geophysics*, **70**, no. 4, V87–V95.
- Yilmaz, Ö., 2001, *Seismic data analysis*: Society of Exploration Geophysicists.

- Yu, C., E. A. Day, M. V. de Hoop, M. Campillo, and R. D. van der Hilst, 2017, Mapping mantle transition zone discontinuities beneath the central pacific with array processing of ss precursors: *Journal of Geophysical Research: Solid Earth*, **122**, 10–364.
- Zhan, Z., Q. Li, and J. Huang, 2018, Application of wavefield compressive sensing in surface wave tomography: *Geophysical Journal International*, **213**, 1731–1743.
- Zhang, J., and T. Zheng, 2014, Receiver function imaging with reconstructed wavefields from sparsely scattered stations: *Seismological Research Letters*, **86**, 165–172.
- Zwartjes, P., and M. Sacchi, 2007, Fourier reconstruction of nonuniformly sampled, aliased data: *Geophysics*, 72: V21–V32.